The Astrophysical Journal, 879:70 (16pp), 2019 July 10 https://doi.org/10.3847/1538-4357/ab22a2

Near-infrared Spectroscopy of Galaxies During Reionization: Measuring C III] in a Galaxy at $z = 7.5$

Taylor A. Hutchison[1,2,9,10], Casey Papovich[1,2], Steven L. Finkelstein[3], Mark Dickinson[4], Intae Jung[3], Adi Zitrin[5], Richard Ellis[6], Sangeeta Malhotra[7,8], James Rhoads[7,8], Guido Roberts-Borsani[6], Mimi Song[7,11], and Vithal Tilvi[8]
[1] Department of Physics and Astronomy, Texas A&M University, College Station, TX 77843-4242, USA; aibhleog@physics.tamu.edu
[2] George P. and Cynthia Woods Mitchell Institute for Fundamental Physics and Astronomy, Texas A&M University, College Station, TX 77843-4242, USA
[3] Department of Astronomy, The University of Texas at Austin, Austin, TX 78712, USA
[4] National Optical Astronomy Observatory, Tucson, AZ 85719, USA
[5] Department of Physics, Ben-Gurion University of the Negev, Be'er-Sheva 8410501, Israel
[6] Department of Physics and Astronomy, University College London, Gower Street, London, WC1E 6BT, UK
[7] Astrophysics Science Division, Goddard Space Flight Center, Greenbelt, MD 20771, USA
[8] School of Earth & Space Exploration, Arizona State University, Tempe, AZ 85287, USA
Received 2019 January 30; revised 2019 April 25; accepted 2019 May 16; published 2019 July 8

Abstract

We present Keck/MOSFIRE *H*-band spectroscopy targeting C III] λ1907, 1909 in a $z = 7.5056$ galaxy previously identified via Lyα emission. We detect strong line emission at $1.621 \pm 0.002\,\mu$m with a line flux of $(2.63 \pm 0.52) \times 10^{-18}$ erg s^{-1} cm^{-2}. We tentatively identify this line as [C III] λ1907, but we are unable to detect C III] λ1909 owing to sky emission at the expected location. This gives a galaxy systemic redshift, $z_{\rm sys} = 7.5032 \pm 0.0003$, with a velocity offset to Lyα of $\Delta v_{\rm Ly\alpha} = 88 \pm 27$ km s^{-1}. The ratio of combined C III]/Lyα is 0.30–0.45, one of the highest values measured for any $z > 2$ galaxy. We do not detect Si III] $\lambda\lambda$1883, 1892, and place an upper limit on Si III]/C III] < 0.35 (2σ). Comparing our results to photoionization models, the C III] equivalent width ($W_{\rm C\,III]} = 16.23 \pm 2.32$ Å), low Si III]/C III] ratio, and high implied [O III] equivalent width (from the *Spitzer*/IRAC [3.6]–[4.5] $\simeq 0.8$ mag color) require subsolar metallicities ($Z \simeq 0.1$–$0.2\,Z_{\odot}$) and a high ionization parameter, $\log U \gtrsim -1.5$. These results favor models that produce higher ionization, such as the BPASS models for the photospheres of high-mass stars, and that include both binary stellar populations and/or an IMF that extends to 300 $M_{\odot}$. The combined C III] equivalent width and [3.6]–[4.5] color are more consistent with ionization from young stars than active galactic nuclei (AGNs); however, we cannot rule out ionization from a combination of an AGN and young stars. We make predictions for *James Webb Space Telescope* spectroscopy using these different models, which will ultimately test the nature of the ionizing radiation in this source.

Key words: cosmology: observations – dark ages, reionization, first stars – galaxies: evolution – galaxies: high-redshift

1. Introduction

One of the most important unknowns in extragalactic astronomy is how reionization occurred. During the Epoch of Reionization ($z \approx 6$–10; EoR), neutral hydrogen (H I) dominated the intergalactic medium (IGM), attenuating radiation from early stellar populations (SPs) and masking galaxies from detection (e.g., Finkelstein 2016; Stark 2016; Dayal & Ferrara 2018, and references therein). Understanding how and when this occurs can reveal whether or not these young galaxies provided the necessary ionizing radiation to completely reionize the IGM by $z \simeq 6$ (inferred from quasar Lyα forests; e.g., Fan et al. 2002; Mortlock et al. 2011; Venemans et al. 2013; McGreer et al. 2015), less than one billion years after the Big Bang.

The physical properties of galaxies during this epoch are not well understood, as only a very small number have been confirmed spectroscopically, with only the brightest sources detected (e.g., Vanzella et al. 2011; Ono et al. 2012; Schenker et al. 2012; Shibuya et al. 2012; Finkelstein et al. 2013; Oesch et al. 2015; Zitrin et al. 2015; Roberts-Borsani et al. 2016; Song et al. 2016; Matthee et al. 2017; Stark et al. 2017; Laporte et al. 2017a, 2017b; Larson et al. 2018; Jung et al. 2019). Due to the galaxies' distances, they are very faint $H_{160} \gtrsim 25$–27 mag, e.g., Finkelstein et al. 2015; Bouwens et al. 2015), with their rest-frame ultraviolet (UV) spectral features pushed out to near-infrared (NIR) wavelengths. By nature of the sensitivity of current ground- and space-based telescopes, sky brightness, and current observing techniques, spectroscopic surveys invariably have a magnitude limit imposed on the sample.

Lyα ($\lambda_0 = 1216$ Å; Lyα) emission is one of the most common rest-frame UV features used to study galaxies at higher redshifts ($z \gtrsim 2$) as it is observed to be very strong in star-forming galaxies (e.g., Shapley et al. 2003). Spectroscopic studies target Lyα-emitting galaxies (LAEs) and Lyman Break galaxies (LBGs), selected from large broad- and narrow-band NIR surveys (e.g., Finkelstein et al. 2013), in order to study the evolution of galaxy properties with redshift. Comparing the Lyα and continuum UV properties of galaxies yields constraints on the Lyα escape fraction (e.g., Hayes et al. 2010), which has been used to argue for increasing ionization in galaxies. In addition, constraints on the Lyα escape fraction have inferred an increasing H I neutral fraction in the IGM at $z > 6.5$, where the neutral gas in the IGM is expected to heavily suppress Lyα emission except in large, ionized bubbles (e.g., Hayes et al. 2011; Treu et al. 2013; Dijkstra 2014;

[9] NSF Graduate Fellow.
[10] NASA Postdoctoral Program Fellow.
[11] TAMU Graduate Diversity Fellow.

Schenker et al. 2014; Tilvi et al. 2014; Stark 2016; Mason et al. 2018; Banados et al. 2018).

However, the observed Lyα emission is heavily dependent upon the spatial distributions of H I, as well as the intrinsic characteristics of its emitting galaxy (e.g., Matthee et al. 2016, 2017; Sobral et al. 2017, and references therein), which makes it a useful line for inferring the properties of the circumgalactic medium (CGM) and the interstellar medium (ISM) when compared to nebular lines (e.g., Møller & Warren 1998; Steidel et al. 2011; Verhamme et al. 2015). However, one of the complications of using Lyα (referenced above) is the resonant scattering due to H I (e.g., Dijkstra 2014, and references therein), often shifting the emission hundreds of km s^{-1} redwards of the galaxy's systemic (or true) redshift. This effect is pronounced in galactic outflows, where the blueshifted portion of the Lyα emission has been absorbed and scattered away from the line of sight, allowing the redshifted (backscattered) Lyα emission to pass through unattenuated (Shapley et al. 2003; Dijkstra 2014; Erb et al. 2014). This redshifting of Lyα can add uncertainty to any intrinsic property inferred for a galaxy when using just Lyα emission (e.g., Hayes 2015), as well as significantly impact the visibility of Lyα. Due to the small number of current significant detections of galaxies during the EoR (see above) determining the systemic redshift of these sources is an active field of study (e.g., Stark et al. 2014, 2015a, 2015b, 2017; Ding et al. 2017; Mainali et al. 2017; Matthee et al. 2017).

Recent studies targeted alternative nebular emission lines to measure the systemic redshift of high-redshift galaxies, and give insight into the galaxies' kinematics and ionization (e.g., Stark et al. 2014, 2017; Ding et al. 2017; Maseda et al. 2017; Matthee et al. 2017). UV lines from metals are the best candidates, with C III] $\lambda\lambda$1907,1909 Å as the most promising (e.g., Stark et al. 2015a, 2015b; Jaskot & Ravindranath 2016; Ding et al. 2017; Matthee et al. 2017). Observations of star-forming galaxies at $1.5 < z < 8$ show that C III] is the strongest UV line after Lyα emission (e.g., Shapley et al. 2003; Erb et al. 2010; Mainali et al. 2017). In addition, at $z \sim 2$ C III] equivalent widths ($W_{\rm C\,III]}$) appear to be larger for lower metallicity galaxies (e.g., Erb et al. 2014; Stark et al. 2014; Nakajima et al. 2018a). With both Lyα and C III] detections, the systemic (C III]) and attenuated (Lyα) redshifts can be compared to shed light on the structure and ionization of the CGM as well as the IGM (Du et al. 2018). Understanding the current sample of distant galaxies detected in more detail will better constrain models and enable a deeper understanding of what can be expected with the next generation of telescopes.

We have begun a spectroscopic study with Keck/MOSFIRE to measure the rest-frame UV emission properties of high-redshift galaxies at $z > 5$, with the intention of understanding the frequency of emission line fluxes (other than Lyα) as a function of galaxy property (including apparent magnitude), and to constrain the physical conditions in the galaxy (galaxy metallicities, ionizing source, etc.). This will inform surveys for spectroscopic redshifts and expectations for forthcoming observations with the *James Webb Space Telescope* (*JWST*). Here, we present the first results from this work, studying the *H*-band spectroscopy of a galaxy at $z > 7$ with a redshift from Lyα, targeting the C III] $\lambda\lambda$1907,1909 emission feature.

The remainder of this work is outlined as follows. In Section 2, we present the observations, data reduction, and calibration. The spectra and identification of C III] lines are presented in Section 3; we discuss the implications of our results in Section 4 and use SP models paired with photoionization simulations to synthesize the spectral energy distribution (SED) of the galaxy. Finally, we summarize our conclusions in Section 5. Throughout, we use absolute bolometric (AB) magnitudes (Oke & Gunn 1983) and adopt a cosmology with $\Omega_M = 0.3$, $\Omega_\Lambda = 0.7$, $\Omega_K = 0.0$, and $h = 0.7$ (where $H_0 = 100\,h$ km s^{-1} Mpc^{-1}) consistent with Planck and local measurements (Planck Collaboration et al. 2016; Riess et al. 2016).

2. Data and Methods

The $z > 7$ galaxies in our sample were all selected using photometry from the Great Observatories Origins Deep Survey (GOODS; Giavalisco et al. 2004) and Cosmic Assembly Near-infrared Deep Extragalactic Legacy Survey (CANDELS; Grogin et al. 2011; Koekemoer et al. 2011) imaging data, combined with photometric redshift measurements and selection methods discussed in Finkelstein et al. (2013, hereafter F13) and Finkelstein et al. (2015). Two of the galaxies targeted in our observations were previously confirmed to have $z > 7$ from spectroscopic measurements of Lyα emission (F13; Jung et al. 2019; hereafter J19). The galaxy featured in this work, z7_GND_42912, was originally spectroscopically confirmed via Lyα with $z_{\rm Ly\alpha} = 7.5078 \pm 0.0004$ by F13. This was confirmed by Tilvi et al. (2016, hereafter T16) using *Hubble Space Telescope* (*HST*) grism spectroscopy. Recently, J19 published an updated redshift of $z_{\rm Ly\alpha} = 7.5056 \pm 0.0007$ using data from >16 hr of total *Y*-band MOSFIRE spectroscopy.[12]

2.1. Observations and Data Reduction

H-band spectroscopic observations of our sample were taken using the Keck/MOSFIRE NIR spectrograph (McLean et al. 2012) for three nights in 2014 and one night in 2017. In addition, we make use of data from an independent observation taken with MOSFIRE in 2016. The dates of observations, total exposure time, average seeing (derived from the final reduced 2D spectrum), and instrument setup are shown in Table 1. For all of the data, a standard dither pattern of ABAB was used, with 0.″7 width slits for all targets in the masks and standard star frames. In each mask, a reference star was placed on a slit to monitor the seeing and atmospheric variability as well as improve the flux calibration process by providing an absolute calibration (see Section 2.2). Due to significant photometric variability, the 2014 March 15 data and parts of the 2014 March 14 data were left out of our analysis (see Appendix A for a description of our seeing and variability map). Ar and Ne arcs were taken, although skylines were used instead for wavelength calibration.

The data were reduced using the MOSFIRE data reduction pipeline (DRP[13]). The DRP produces background-subtracted, rectified, and flat-fielded two-dimensional (2D) spectra and associated 2D variance for each slit within a given mask. The resulting spectral resolution yields 1.63 Å pixel^{-1}, with 0.″18 pixel^{-1} spatially. We visually inspected the reduced 2D

[12] Note that J19 found evidence the Lyα line is asymmetric. They reported a Lyα redshift using a centroid from a skewed Gaussian. As a result their Lyα redshift is systematically different compared to a fit to Lyα using a symmetric Gaussian. The latter gives a redshift $z_{\rm Ly\alpha} = 7.5072 \pm 0.0003$, consistent with the original value from F13, who also used a symmetric Gaussian.

[13] http://keck-datareductionpipelines.github.io/MosfireDRP/

Table 1
Keck I Observations Using the MOSFIRE NIR Spectrograph

Observation Date	PI	Band	Seeing	t_{exp}	Slit Width[a]	Dithering Pattern	Stepsize	Reference Star		
			(arcsec)	(hr)	(arcsec)		(arcsec)	α	δ	H_{160}
(1)	(2)	(3)	(4)	(5)	(6)	(7)	(8)	(9)	(10)	(11)
2017 Apr 18	Papovich	*H*	0.7	3.711	0.7	ABAB	1.50	189.304712	+62.269859	17.29
2016 May 4	Zitrin[b]	*H*	0.65	1.988	0.7	ABAB	1.25	189.105720	+62.234683	15.99
2014 Mar 25	Malhotra	*H*	0.8	0.994	0.7	ABAB	1.25	189.287154	+62.297020	17.12
2014 Mar 15	Finkelstein	*H*	1.0	1.392[c]	0.7	ABAB	1.25	189.287154	+62.297020	17.12
2014 Mar 14	Finkelstein	*H*	0.6	1.789[c]	0.7	ABAB	1.25	189.287154	+62.297020	17.12

Notes. (1) UT Date of observation. (2) PI of Keck observing program. (3) MOSFIRE NIR band observed. (4) Average seeing derived from the final reduced images of the star in the mask. (5) Total exposure time of the mask. (6) Slit widths in the mask. (7) Dithering pattern of the instrument. (8) Stepsize of the dithering. (9)–(11) R.A. (decimal degree), decl. (decilmal degrees), and H_{160} magnitude of the Reference Star in the mask.
[a] Standard MOSFIRE slit width: $0\farcs7$.
[b] Data not used in final spectral coadd.
[c] Much of the 2014 Mar 14–15 data are taken under poor conditions and unusable. We include only data from 2014 Mar 14 taken from 08:20–09:35 UTC and no frames from 2014 Mar 15 (see Appendix A).

spectra at the potential positions of UV emission lines (such as the C III] doublet) for our galaxies.

2.2. Optimized 1D Extraction and Flux Calibration

We extracted 1D spectra for our sources at the position of an observed emission feature or at the expected center of the slit with an extraction box width of 7 pixels ($1\farcs26$). We used an optimized extraction technique that weights by the inverse-variance and the expected spatial profile of the source to maximize the signal-to-noise ratio (S/N) of the extraction (Horne 1986). As there was no continuum detected for any of our high-redshift sources, we used the wavelength-dependent spatial profile of the reference star in our mask to account for any seeing variations as a function of wavelength (see, Song et al. 2016; Stark et al. 2017).

We applied the identical optimized extraction method for all sources and standard stars to provide consistency. Figure 1 shows a comparison of the optimized method versus the traditional "boxcar" (uniform) extraction for the reference star in our 2017 mask. The spectra shown are pre-flux calibration and telluric correction. The inset, Figure 1(b), shows the spatial profile of the reference star, along with the defined 7 pixel aperture and the series of weights, centered on the peak of emission, used to increase the S/N of the extracted spectra. The weights are made such that at each wavelength step they sum to unity. Figure 1(c) shows that the optimized-extraciton technique increases the S/N by only ∼10%. However, this is expected for spectra with medium-to-high S/N, as the improvement in S/N is greatly enhanced for objects with much lower S/N (see, e.g., Horne 1986).

To derive errors on the 1D spectra, we developed a method which takes advantage of multi-slit observations targeting faint objects (where some or many slits may result in nondetections). The method is described fully in Appendix B. In brief, we chose regions spatially along the mask devoid of a signal or negative traces and extracted "blank" apertures following the same optimized extraction as used on our targets. After gathering at least $N = 20$ of these apertures, we determined the standard deviation of the distribution of the "blank" 1D spectra at each wavelength step as the error. The final 1D error spectrum was then used for all objects in the mask.

For the absolute flux calibration of the spectra we followed two steps. First, we corrected the data for telluric absorption and instrument response using the longslit (2014 data) or spectrophotometric "long2pos" (2017 data) observations of the standard star HIP 53735 (2014 data) and HIP 56147 (2017 data). Both stars have spectral type A0V, and were taken immediately before (2014 data) or in the middle of (2017 data) the observing block for each mask observation. As there were no *H*-band standard star frames taken on 2014 March 25, we used those taken on 2014 March 14 (but we refine the flux calibration in the second step, see below).

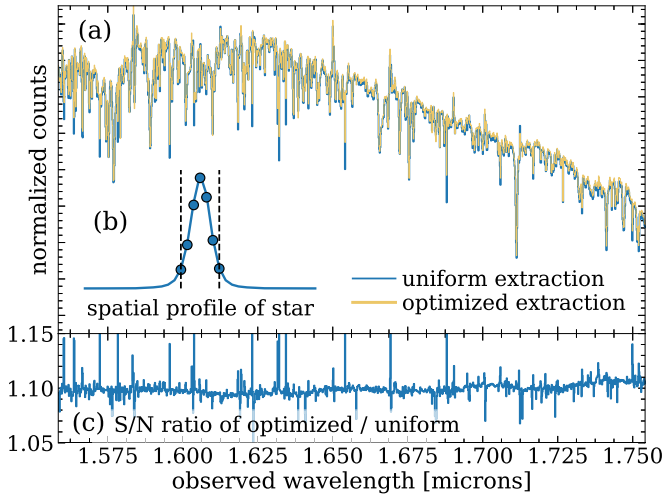

Figure 1. Comparison of the optimized 1D spectral extraction technique vs. traditional uniform extraction for the alignment star in the 2017 April 18 mask. The top panel shows (a) the spectrum extracted using a uniform aperture and the optimized method (as labeled in the plot inset), and (b) the weight used by the optimized process, defined within the 7 pixel extraction aperture, centered on the peak of emission (spatially). The bottom panel (c) shows the ratio of the S/N of the extracted spectra for the optimized method vs. the uniform extraction. There is an overall increase in recovered S/N for the optimized extraction.

Second, we used the reference star in each science mask to refine the absolute flux calibration. This accounts for any variation in seeing or atmospheric transmission between the observation of the spectrophotometric standard and the science mask. We first fit Kurucz models (Kurucz 1993) to the fluxed spectrum of the reference star from our MOSFIRE mask, and use this to extrapolate the spectrum over the entire wavelength range covered by the *HST*/WFC3 F160W bandpass. We then measured a synthetic F160W magnitude by integrating the

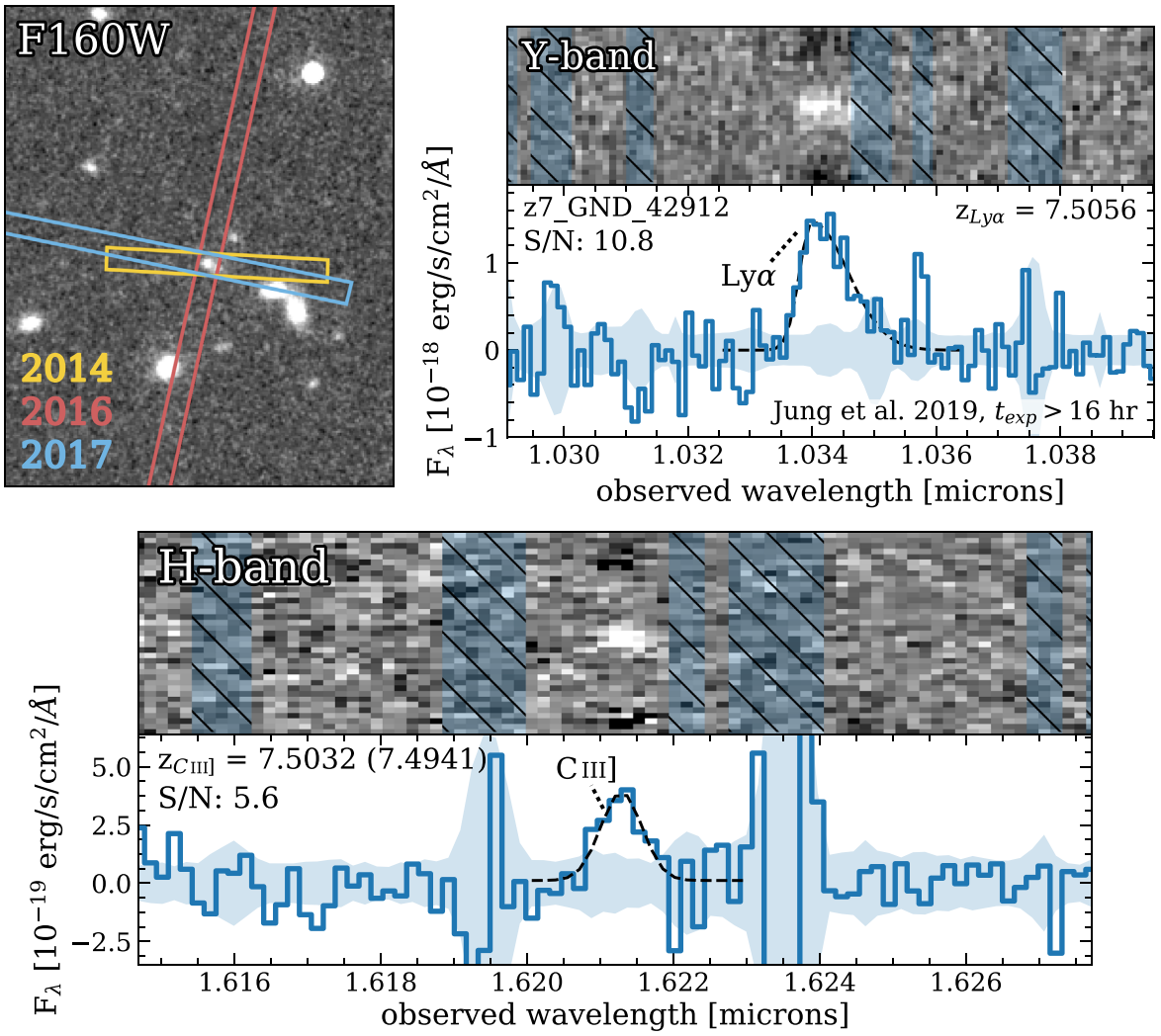

Figure 2. Top left: a zoom in of the CANDELS/GOODS-N field in F160W band, centered on z7_GND_42912. The different colored slits indicate the different data sets and their respective positions on the target. Top right: *Y*-band MOSFIRE spectroscopy of z7_GND_42912 from Jung et al. (2019), showing the 2D S/N spectrum (where the S/N spectrum is the flux divided by the error; the blue hatched regions mask skylines), and the optically extracted 1D spectrum (solid blue line) with error (shaded blue region). The black dashed line shows a (skewed) Gaussian fit to the line. Bottom: *H*-band MOSFIRE spectroscopy showing the combined 2D smoothed S/N spectrum (top panel) and the optimally extracted 1D spectrum from the combined data set (bottom panel). The blue shading is the same as in the top right panel. The black dashed line shows a Gaussian fit to the line.

MOSFIRE spectrum of the star with the F160W bandpass, and fit a scale factor to adjust this to match the (measured) total magnitude in the CANDELS photometry, using the catalog of S.L. Finkelstein et al. (2019, in preparation). We then applied the same scale factor to the corrected MOSFIRE spectra for the galaxies in our sample to derive their absolute flux scaling. We repeated this step for each mask. We then measured the mean of the individual 1D spectra for each galaxy from each mask, weighting by the total exposure time of each mask.

3. Results

z7_GND_42912 (né z8_GND_5896, also known as FIGS_GN1_1292) is a bright (H_{160} = 25.38, Finkelstein et al. 2019, in preparation), highly star-forming galaxy at $z_{Ly\alpha}$ = 7.5078. The brightest detection in our *H*-band sample of high-redshift galaxies, z7_GND_42912, was first spectroscopically confirmed via Lyα emission by F13. Figure 2 shows a portion of the *HST*/WFC3 F160W image of the CANDELS/GOODS-N field, including the MOSFIRE slit positions from the MOSFIRE 2013, 2014, and 2017 observing runs. Figure 2 also shows the *Y*-band and *H*-band 2D and 1D combined spectroscopy of this galaxy.

3.1. Reanalysis of the Lyα Emission

The top right of Figure 2 shows the >16 hr *Y*-band 2D and 1D spectra from J19, centered on the observed Lyα emission. The top panel shows the 2D *Y*-band S/N spectrum (i.e., the image of the flux divided by the error), with skylines masked out. The bottom panel shows the corresponding 1D *Y*-band flux spectrum with the blue-shaded regions denoting the error.

As discussed in F13, the profile of the Lyα emission appeared symmetric, atypical (but not unseen) for Lyα emission at higher redshifts (e.g., Dijkstra 2014, 2017; Erb et al. 2014), where generally the blue half of the emission line has been absorbed and scattered by H I in the IGM. The more recent analysis of J19 used >16 hr of MOSFIRE *Y*-band data and shows an asymmetric Lyα line profile (although the uncertainties do not rule out that the line is symmetric). With this reported asymmetry, it could indicate a larger offset

Table 2
Measurements for z7_GND_42912

$z_{Ly\alpha}$	z_{sys}	Line	λ_0 (Å)	λ_{obs} (μm)	f_{line} (10^{-18} erg^{-1} s^{-1} cm^{-2})	$W_{line,0}$ (Å)	Reference
(1)	(2)	(3)	(4)	(5)	(6)	(7)	(8)
7.5078 ± 0.0004	⋯	Lyα	1215.67	1.03427 ± 0.00005	2.64 ± 0.74[a]	7.5 ± 1.5[b]	Finkelstein et al. (2013)
7.512 ± 0.004	⋯	Lyα	1215.67	1.035 ± 0.005	10.6 ± 1.9	49.3 ± 8.9[b]	Tilvi et al. (2016)
7.510 ± 0.003	⋯	Lyα	1215.67	1.033 ± 0.004	11.0 ± 1.7		Larson et al. (2018)
7.5056 ± 0.0007[c,d]	⋯	Lyα	1215.67	1.0340 ± 0.0001	14.6[d] ± 1.4	33.2 ± 3.2[b]	Jung et al. (2019)
	7.5032 ± 0.0003	[C III]	1906.68	1.62129 ± 0.00006	2.63 ± 0.52	16.23 ± 2.32[e]	This work
	⋯	C III]	1908.73	⋯	1.74 ± 0.35[f]		This work
	⋯	Si III]	1882.47	⋯	<0.924 (2σ)		This work
	⋯	Si III]	1892.03	⋯	⋯		This work

Notes. (1) Redshift derived from Lyα. (2) Systemic redshift derived from [C III]. (3) Spectroscopic line measured. (4) Rest-frame wavelength of line. (5) Observed wavelength for line. (6) Line flux. (7) Rest-frame equivalent width. (8) Reference for a given row of measurements.
[a] The previous lower line flux resulted from an earlier discrepancy, which has been resolved and updated as described in Jung et al. (2019) (see also Section 3.1).
[b] The differences in Lyα equivalent width in the literature result from the revised Lyα line flux (see Jung et al. 2019 and Section 3.1) and updates to the CANDELS photometry (Finkelstein et al. 2019, in preparation). There are also additional differences that stem from the methods used to analyze *HST*/grism data (Tilvi et al.) compared to the MOSFIRE data (Jung et al.).
[c] Redshift derived from asymmetric fit to Lyα profile.
[d] Values for Lyα used in the analysis in this work.
[e] Based on the identification of the emission line as [C III] λ1907.
[f] Line flux inferred by using a [C III] / C III] ratio of 1.5 ± 0.1. Note ratio also has a systematic uncertainty of 7% depending on electron density and temperature, see Section 4.1.

between the Lyα emission and systemic redshift for this galaxy. However, this interpretation is not unique, as some $z > 6$ sources show both an asymmetric Lyα line profile with a small offset from the systemic redshift (e.g., Stark et al. 2015a).

Deep (40-orbit) *HST*/WFC3 G102 observations were taken for this galaxy as part of the Faint Infrared Grism Survey (FIGS; Pirzkal et al. 2017). Using a portion of the FIGS data, T16 showed that while the location of the Lyα emission matched well between those observations and F13, the measured Lyα line flux was a factor of ∼4 higher for the grism data (see Table 1 of T16). Using the full FIGS data set, Larson et al. (2018) measured a Lyα line flux consistent with those of T16. However, it is important to note that with the revised flux calibration for the 2013 April 18 *Y*-band data (J19), this discrepancy disappears and becomes consistent with the grism measurement, within errors.[14] The remaining differences between the equivalent width of Lyα, $W_{Ly\alpha}$, measurements for the two data sets arise from the different techniques applied to these independent data to calculate this value. Here, we adopt the Lyα line flux and redshift from J19 (see Table 2).

3.2. Analysis of the C III] Emission

Based upon the Lyα redshift, the expected location of the C III] λλ1907,1909 lines would be within a few hundred km s^{-1} of 1.622 μm and 1.624 μm, respectively. For each *H*-band data set, we visually inspected the spectra in this wavelength range. The bottom panel of Figure 2 shows the 2D and 1D spectral region of the expected location of the C III] lines. We identified an emission line in this region at 1.6213 μm, which we label as one of the C III] lines. We fit a Gaussian to the 1D spectrum for the observed C III] emission line, from which we derive a line flux of (2.63 ± 0.52) $\times 10^{-18}$ erg s^{-1} cm^{-2}, at S/N = 5.6. We also inspected the spectrum over the full wavelength range, but failed to identify any other candidate emission line.

In addition, we verified the detection of this line using data taken for this galaxy from an independent MOSFIRE program from 2016 May 4 (PI Zitrin, see Table 1). We reduced the data following the same steps as discussed above in Section 2.2. However, these data lacked a telluric standard observation. Therefore, we make no attempt to calibrate the spectrum, but these data provide a robust, independent detection of the line. Figure 3 shows the *H*-band 2D smoothed S/N spectrum and 1D optimally extracted flux spectrum of the 2016 data. We identify an emission line at the same wavelength as the detected C III] with a S/N of 2.7. This provides additional confidence in the detection of this emission line.

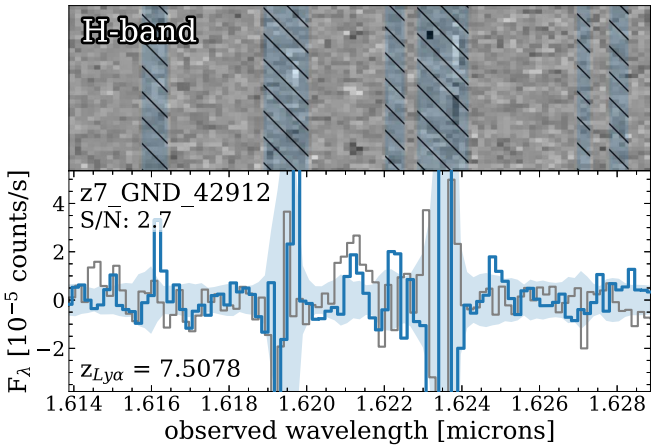

Figure 3. *H*-band MOSFIRE spectroscopy from the 2016 May 4 data of z7_GND_42912 showing an independent detection of C III] emission. The data are not flux calibrated. The top panel shows the 2D smoothed S/N spectrum, with the blue hatched regions masking out skylines; the bottom panel shows the optimally extracted 1D flux spectrum, shaded blue regions indicating the error. Overplotted in gray is the 1D co-added and flux-calibrated spectrum from Figure 2, scaled to be visible.

[14] In brief, the c. 2013 version of the MOSFIRE DRP provided different units (not in the original documentation) between the multi-object spectral frames and the longslit standard star frames. This has been corrected.

In order to determine the systemic redshift, we need to assign an identification to this line. As mentioned before, C III] is represented as a doublet[15] with a rest-frame separation of ∼2 Å, which for the redshift of this galaxy corresponds to an observed separation of ∼16 Å. Due to the wavelength of the observed line, in both cases ([C III] λ1907 or C III] λ1909) the expected location of the other line falls on one of the two strong skylines adjacent to the emission feature (see the *H*-band 2D spectrum in Figure 2). This prevents us from making a robust identification, as the other line is unobservable in both cases. We discuss this complication and its implications in more detail in Section 4.1.

In addition to C III], the Si III] λ1883,1892 doublet would also fall in the MOSFIRE *H*-band spectrum. This line is observed in some high-redshift galaxies, with a typical flux ratio of (Si III] λ1883)/([C III]+C III]) = 0.1–0.3 (e.g., Stark et al. 2014; Patrício et al. 2016; Steidel et al. 2016; Berg et al. 2018). We therefore inspected the 2D spectra for signs of the these lines, but failed to identify any line at the expected location of Si III]. We forced a Gaussian fit for Si III] lines at the expected wavelengths, using the location and width of the C III] line. This places a formal 2σ upper limit of Si III] $\lambda1883 < 0.92\ (1.08) \times 10^{-18}$ erg s^{-1} cm^{-2}, assuming the observed emission is [C III] λ1907 (C III] λ1909). These results imply a (Si III] λ1883)/(C III] λ1907) ratio of <0.35 (2σ), and a (Si III] λ1883)/([C III]+C III]) ratio of <0.21 (2σ). We discuss this in more detail below in Section 4.2.

3.3. Implications for Nebular Emission from the IRAC [3.6]–[4.5] Color

Apart from C III], this galaxy also shows evidence of additional, strong emission lines in the colors of the galaxy's SED. From F13, the reported Infrared Array Camera (IRAC) color was found to be very red, with [3.6]–[4.5] = 0.98 mag. Using updated photometry, this color is revised downward to [3.6]–[4.5] $= 0.77^{+0.23}_{-0.28}$ mag (Finkelstein et al. 2019, in preparation; although consistent with the photometric errors of F13). z7_GND_42912 has a high star formation rate (SFR) of $180^{+20}_{-50}\,M_\odot$ yr^{-1} from the analysis of the full SED (J19). The interpretation of the red IRAC color suggests the galaxy has strong nebular emission from Hβ + [O III] in the 4.5 μm band with an inferred rest-frame [O III] λ5007 equivalent width ($W_{[O\,III]}$) of ∼600 Å (F13, Finkelstein et al. 2019, in preparation; following the prescription of Papovich et al. 2001). F13 used the strength of this emission to constrain the metal abundance of z7_GND_42912 (≃0.2–0.4 $Z_\odot$) and its relatively young inferred age (10 Myr). In the discussion below, we will use both the implied [O III] equivalent width from the red IRAC color and our C III] measurement to study the ionization conditions and metallicity of this galaxy (see Section 4.2).

4. Discussion

4.1. Systemic Redshifts and Implications for Lyα

Unlike Lyα (which is subject to strong resonant scattering), the C III] nebular emission line provides a measure of the systemic redshift of a galaxy. This can be used to measure the velocity offset of Lyα ($\Delta v_{Ly\alpha}$) from the systemic, which then provides insight into the kinematics of a galaxy (e.g., Erb et al. 2014; Stark et al. 2017) and information about the Lyα escape fraction (e.g., Hayes 2015).

In the case of z7_GND_42912, we detect one of the lines in the C III] doublet with a S/N of 5.6. In order to determine which line we have detected, we took into account the implied $\Delta v_{Ly\alpha}$ derived from the systemic assuming each of the possible lines. Figure 4 shows the expected location of the other line assuming the detected emission is (a) [C III] λ1907 or (b) C III] λ1909. As discussed above (Section 3), in both cases the other line of the C III] doublet would be located in a region with strong night sky emission. The velocity offset for the case that the line is C III] λ1909 is $\Delta v_{Ly\alpha} = 410 \pm 27$ km s^{-1}. The velocity offset for the case that the line is [C III] λ1907 is $\Delta v_{Ly\alpha} = 88 \pm 27$ km s^{-1}.[16] These reported velocity offsets have been corrected to the heliocentric frame, with the Lyα and C III] data sets having mean corrections of −7.79 km s^{-1} and −11.57 km s^{-1}, respectively (McLinden et al. 2011; Chonis et al. 2013; Song et al. 2014). It is important to note that while we apply this correction to the velocity offsets, we do not correct the redshifts listed in Table 2.

The value of $\Delta v_{Ly\alpha}$ has implications for kinematics, outflows, and geometry in z7_GND_42912. From a study of mid-redshift ($z \simeq 2$–3) star-forming galaxies, Erb et al. (2014) suggest a correlation exists between $\Delta v_{Ly\alpha}$ and UV luminosity, while an anticorrelation exists between $\Delta v_{Ly\alpha}$ and Lyα equivalent width. Erb et al. argue these are a consequence of changing the column density, covering fraction, and/or velocity dispersion of gas within the ISM—all effects found to impact the emergent profile of Lyα emission (Verhamme et al. 2006; Dijkstra 2014). The distribution of $\Delta v_{Ly\alpha}$ is also expected to decrease for increasing redshift (Schenker et al. 2013; Choudhury et al. 2015; Stark et al. 2015a), implying an emergence of harder ionizing radiation fields that can blow out a substantial fraction of neutral gas in the ISM. This clearing of gas would mean that Lyα photons can escape into the (neutral) IGM (this has additional implications for the leakage of ionizing Lyman continuum photons, e.g., Kimm et al. 2019).

Figure 5 shows a compilation of rest-frame UV absolute magnitude versus $\Delta v_{Ly\alpha}$ for galaxies in the literature at $z > 6$ and $z \sim 2$–3. One point immediately evident from the figure is that few galaxies have high $\Delta v_{Ly\alpha}$, with a mode of the distribution (i.e., the typical value) of ≃200 km s^{-1}. At $z \sim 2$–3, studies of LAEs find very few galaxies at all UV luminosities with $\Delta v_{Ly\alpha} > 300$ km s^{-1}. At $z > 6$, the only galaxies with high $\Delta v_{Ly\alpha} > 350$ km s^{-1} have $M_{UV} < -22.5$ mag (e.g., Willott et al. 2015; Stark et al. 2017). All galaxies with luminosities fainter than $M_{UV} > -22.4$ mag, have lower $\Delta v_{Ly\alpha}$ (see, Stark et al. 2017).

z7_GND_42912 has $M_{UV} = -21.58$ (J19). Comparing z7_GND_42912 to other galaxies in Figure 5, we favor the interpretation that the line is [C III] λ1907. This is consistent with the distribution of other galaxies, and implies the lower value of $\Delta v_{Ly\alpha}$ for z7_GND_42912 ($\Delta v_{Ly\alpha} = 88 \pm 27$ km s^{-1}), corresponding to a systemic redshift $z_{sys} = 7.5032 \pm 0.0003$. In this case, as described above, a harder ionization field would likely be responsible for clearing H I around the galaxy, allowing Lyα to escape closer to z_{sys} (Schenker et al. 2013; Stark et al. 2015a, 2017).

[15] Strictly speaking, C III] is a line pair (see, e.g., Stark et al. 2014), a combination of one forbidden and one semiforbidden transition—namely [C III] λ1906.68 and C III] λ1908.73. When applicable, we will reference the individual lines using the notation [C III]λ1907 and C III]λ1909, respectively.

[16] Due to the asymmetric fit of the Lyα emission, there exists an additional possible systematic uncertainty associated with the centering of this emission line, where a more symmetric fit would result in a ∼70% increase in the measured $\Delta v_{Ly\alpha}$.

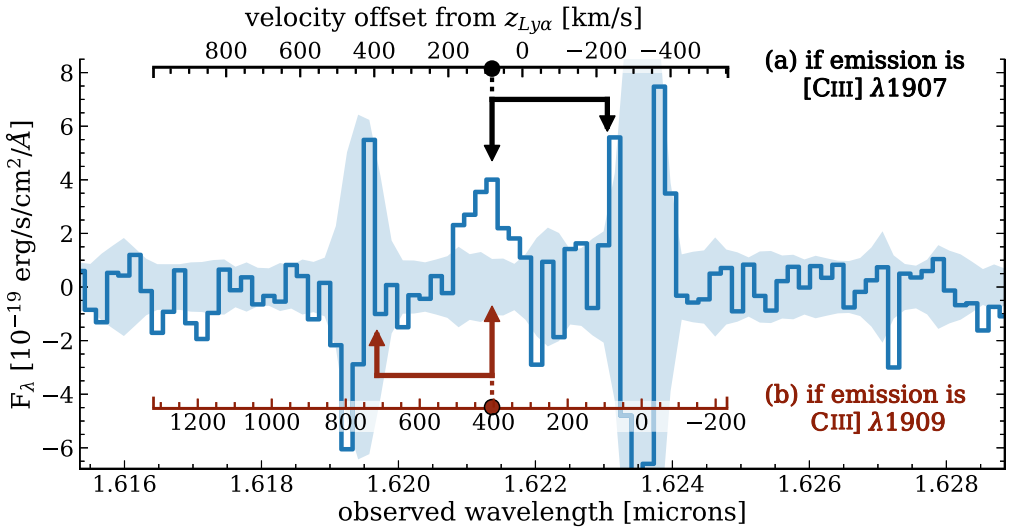

Figure 4. Systemic redshift determination for z7_GND_42912 for the case that the detected emission line is (a) [C III] λ1907 or (b) C III] λ1909 as a function of both wavelength and velocity offset from $z_{Ly\alpha}$. The black and red arrows indicate the expected location of both lines of the C III] emission doublet for case a: the identified line is [C III] λ1907, and case b: the identified line is C III] λ1909, respectively. The inset axis shows the velocity offset of Lyα from the systemic for each possible C III] identification, and the arrows show the expected location of the other line of the doublet (in both cases they would fall on sky emission lines).

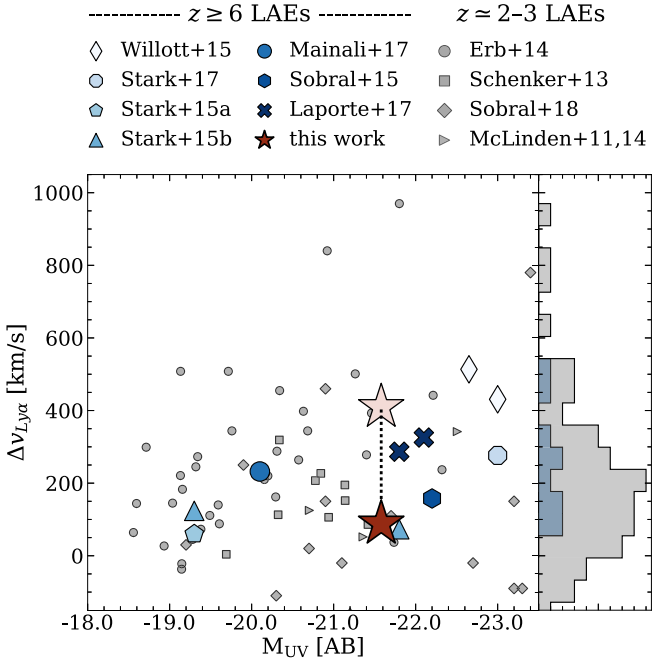

Figure 5. A compilation of velocity offsets for galaxies at $z \geq 6$ with both Lyα and a nebular line (which provides the systemic redshift of the source). In addition, we have included a sample of galaxies at $z \approx 2$–3 from Erb et al. (2014), Schenker et al. (2013), Sobral et al. (2018), McLinden et al. (2011), and McLinden et al. (2014), respectively. The stars represent z7_GND_42912 where the dark (light) star assumes the detected emission is [C III] λ1907 (C III] λ1909).

Additional evidence in support of the [C III] λ1907 interpretation comes from studies of "green pea" galaxies at $z \sim 0.1 - 0.3$. Using a sample of 43 green pea galaxies, Yang et al. (2017) find a correlation between Lyα equivalent width and Lyα escape fraction. Furthermore, they find that galaxies with lower $\Delta v_{Ly\alpha}$ and lower dust attenuation show larger values of Lyα escape fraction. Given the relatively high Lyα equivalent width and lower dust attenuation of z7_GND_42912 (F13, J19), this provides additional support for a lower $\Delta v_{Ly\alpha}$, and supports that the observed emission line is [C III] λ1907.

However, while we identify the emission line as [C III] λ1907, we are unable to rule out that the detected line is C III] λ1909. We therefore consider both possibilities in the discussion that follows. Future observations of other nebular emission lines will test this interpretation (e.g., from *JWST*, see Section 4.3 below).

Lastly, we estimated the total flux of the combined [C III] λ1907 + C III] λ1909 lines in order to compare to previous results and models. Many previous studies are unable to resolve these lines. The C III] doublet is also blended in the spectra output from some radiative transfer codes (e.g., CLOUDY). To estimate the total flux, we use models for the [C III]/C III] ratio (see Section 4.2), combined with the line flux we measure. This is similar in practice to methods used in the study of other galaxies at $z > 1$ (e.g., Sanders et al. 2016; Maseda et al. 2017) in the case that only part of the C III] doublet is identified (e.g., Stark et al. 2015a). For a range of gas densities 10^2–10^4 cm^{-3}, the [C III]/C III] ratio varies from ∼1.5–1.2 (Maseda et al. 2017). For an electron density of 300 cm^{-3} (see Section 4.2), our models return a ratio of 1.5 (with a range of 0.1, depending upon electron density and temperature) for all metallicities considered ($Z = 0.05$–$0.5\ Z_\odot$). This is consistent with previous work to within 10% (e.g., Stark et al. 2015a; Maseda et al. 2017). Therefore, we adopt this ratio ([C III] λ1907)/(C III] λ1909) = 1.5 for all calculations. The detected emission line has a flux of $F_{\rm Line} = (2.6 \pm 0.5) \times 10^{-18}$ erg s^{-1} cm^{-2} (independent of line identification). For the case that the detected emission line is [C III] λ1907, this yields a total line flux of $(4.4 \pm 0.8) \times 10^{-18}$ erg s^{-1} cm^{-2}, corresponding to a rest frame $W_{\rm C\,III]} = 16.23 \pm 2.32$. These measurements are summarized in Table 2. For the alternative case that the detected emission line is C III] λ1909, the total line flux would be higher by approximately 50%, $(6.6 \pm 1.3) \times 10^{-18}$ erg s^{-1} cm^{-2}, and would correspond to $W_{\rm C\,III]} = 25.09 \pm 2.32$.

Using the combined total line flux for [C III]+C III], Figure 6 compares the relationship between the (total) C III] and Lyα emission for z7_GND_42912 to other galaxies with line measurements at $z \geq 6$ (using Matthee et al. 2017, and

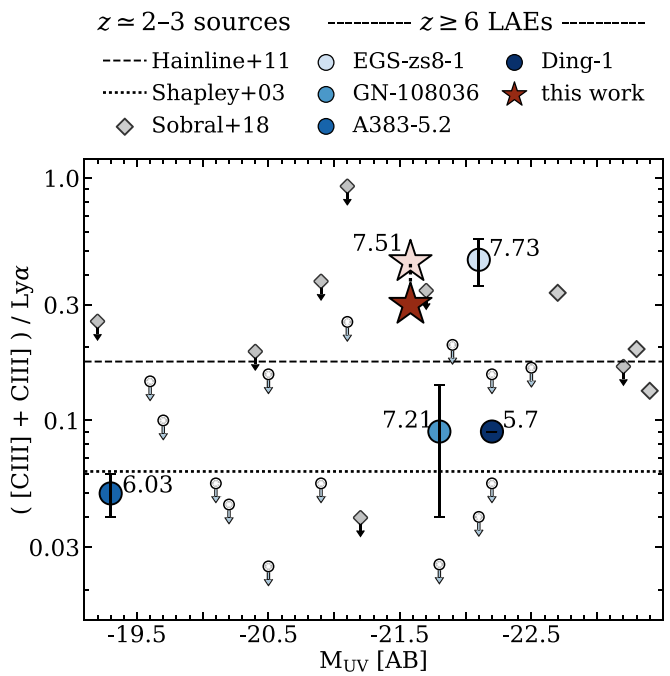

Figure 6. All measured $z \geqslant 6$ galaxies with spectroscopic measurements in both Lyα and C III] from the compilation in Matthee et al. (2017, and references therein). 1σ upper limits are shown as open circles with arrows, while the detections are colored circles. The $z_{\mathrm{Ly}\alpha}$ of the detections are shown next to the points. The stars represent z7_GND_42912 where the dark (light) star assumes the detected emission is [C III] λ1907 (C III] λ1909). In addition, we have included a sample of $z \approx$ 2–3 LAEs from Sobral et al. (2018), represented by the gray diamonds and 1σ diamond upper limits. The dashed line represents the $z \sim 3$ UV-selected AGN composite from Hainline et al. (2011) and the dotted line represents the $z \sim 3$ LBG composite from Shapley et al. (2003).

references therein). For z7_GND_42912, we measured a ([C III]+C III])/Lyα ratio of 0.30 $\pm$ 0.04. Most measurements in the literature provide only upper limits on C III] (shown in the figure as arrows) while there are a handful of detections (shown in the figure as circles). z7_GND_42912 has one of the highest C III]/Lyα ratios yet measured during this epoch (and this would be even higher in the case where the line is C III] λ1909). (We note that using the *HST* grism Lyα line flux (see Table 2) would increase this ratio by $\simeq$40%.) From these results, there does not seem to be any significant trend between the ratio of ([C III]+C III])/Lyα and redshift or M_{UV}, although the sample size is still too small for robust conclusions. This apparent randomness is not unexpected, as the emergent Lyα emission measured in these sources may be subject to different effects. Therefore, it is not immediately clear if the ([C III] +C III])/Lyα ratio is indicative of the ionization state of these galaxies, however this ratio could be investigated as an interesting probe of these sources.

4.2. Physical Interpretation of the Emission Lines

For z7_GND_42912, the ([C III]+C III])/Lyα flux ratio and red [3.6]–[4.5] color suggest high ionization. Several studies have argued that these red IRAC [3.6]–[4.5] colors for galaxies in the reionization era imply strong nebular emission from Hβ +[O III], redshifted into the IRAC bandpasses (e.g., Smit et al. 2015; Roberts-Borsani et al. 2016; Matthee et al. 2017; Stark et al. 2017). This is the case for z7_GND_42912, with [3.6]–[4.5] = 0.77 mag, which implies a rest-frame [O III] equivalent width ($W_{[\mathrm{O\ III}]}$) of $\simeq$ 600 Å (see above). As has been shown at lower redshifts ($z \sim 2$), higher values of $W_{[\mathrm{O\ III}]}$ have been found to correlate closely with an increasing ionizing efficiency (Tang et al. 2018). This may be responsible for ionizing a significant fraction of the ISM, therein ionizing a substantial amount of H I and allowing a higher Lyα escape fraction.

We investigated the properties of z7_GND_42912 by calculating the nebular emission spectrum expected assuming different SP models, with variable ionization, hydrogen gas density, stellar and nebular metallicities, and other parameters (motivated by analyses of other galaxies in the literature, e.g., Inoue 2011; Stanway et al. 2014; Jaskot & Ravindranath 2016; Sanders et al. 2016; Steidel et al. 2016; Byler et al. 2017; Stark et al. 2017; Strom et al. 2017; Byler et al. 2018; Sobral et al. 2018). To study model-dependent systematic differences in the nebular emission spectrum, we used a variety of SPs that also vary the IMFs (including variations to the upper mass cut-off of the IMF, $M_{\mathrm{IMF}}^{\mathrm{up}}$) in order to test a large range of available parameter-space (e.g., Steidel et al. 2016).

We used the Binary Population and Spectral Synthesis v2.0 (BPASS; Eldridge et al. 2017) and Starburst99 (S99; Leitherer et al. 2014) models with continuous star formation histories (SFHs) of 1 $M_{\odot}$ yr^{-1} with similar metallicity to z7_GND_42912 (0.2–0.4 $Z_{\odot}$; based upon F13 values), varying the age from 10, 30, and 100 Myr (an age of 10 Myr is within the age range derived from fitting models to the broad-band colors for this galaxy by Finkelstein et al. 2015 and J19). In order to test different models for the photospheres of massive stars and to allow the effects of binary SPs, we used both the single-star and binary-star SP models provided by BPASS. The S99 SPs use Geneva 2012/13 stellar tracks assuming zero rotation, and cover a slightly different range of metallicity compared to the BPASS models (see Table 3).

We used the radiative transfer and photoionization micro-physical code CLOUDY v17.0 (Ferland et al. 2017) to produce the nebular emission spectrum for each SP. We modeled both the case where the nebular gas metallicity is fixed to be the same as the SP, and also the case where the nebular gas metallicity is allowed to vary from 0.3 to 0.5 $Z_{\odot}$ independent of the metallicity of the SP. To normalize the ionizing continuum, we chose a range of ionization parameters, defined as the ratio of the number density of ionizing photons to the number density of the gas, ($U \equiv n_{\gamma}/n_{H}$), running from log $U = -3.5$ to -1.5 in steps of 0.2 dex, assuming a covering factor ($\Omega/4\pi$) of 1. Per the methods followed in Steidel et al. (2016), we set the total gas density (n_H) to 300 cm^{-3}. We assumed no attenuation by dust in the CLOUDY models, however we postprocess the model outputs to include dust attenuation assuming a foreground dust screen (Calzetti et al. 2000) with the reported color excess $E(B-V) = 0.22$ for z7_GND_42912 (J19). We assume solar elemental abundances in all of our modeling, but see below. Table 3 lists the full range of models and parameters used in our CLOUDY modeling.

In order to investigate the range of model parameter space that can reproduce the observed properties of z7_GND_42912, we focus on the total C III] rest-frame equivalent width ($W_{\mathrm{C\ III]}}$; see Table 2) and the observed IRAC [3.6]–[4.5] color, which provides a measure of the Hβ + [O III] equivalent width. The values for the implied $W_{[\mathrm{O\ III}]}$ $\sim$600 Å and total $W_{\mathrm{C\ III]}}$ are consistent with the relations seen in low metallicity dwarf galaxies at low redshifts, which show correlations between these quantities, and favor high ionization and lower metallicity

Table 3
Full List of CLOUDY Parameters Used in Simulations

	Parameter	BPASS SPs	Starburst99 SPs	AGNs
(1)	Z_* [$Z_\odot$]	0.1, 0.2, 0.3, 0.5	0.05, 0.1, 0.4	⋯
(2)	$Z_{\rm neb}$ [$Z_\odot$]	$= Z_*$ 0.3, 0.5	$= Z_*$ 0.3, 0.5	0.05, 0.1, 0.2, 0.3, 0.4, 0.5
(3)	n_H [cm^{-3}]	300	300	300
(4)	log U	[−3.5, −1.5], steps of 0.2	[−3.5, −1.5], steps of 0.2	[−3.5, −1.5], steps of 0.2
(5)	$\Omega/4\pi$	1.0 ($\Omega = 4\pi$)	1.0 ($\Omega = 4\pi$)	open ($\Omega \ll 4\pi$)
(6)	$M_{\rm IMF}^{\rm up}$ [$M_\odot$]	100, 300	100	⋯
(7)	α	−1.30; [0.1, 0.5)$M_\odot$ −2.35; [0.5, $M_{\rm IMF}^{\rm up}$] $M_\odot$	−1.30; [0.1, 0.5) $M_\odot$ −2.30; −2.00; −1.70; } [0.5, $M_{\rm IMF}^{\rm up}$] $M_\odot$	⋯ table agn[a]
(8)	SFH [$M_\odot$ yr^{-1}]	continuous; 1.0	continuous; 1.0	⋯
(9)	Age [Myr]	10, 30, 100	10, 30, 100	⋯

Note. (1) Stellar metallicity of the SPs, Z_*. (2) Nebular metallicity used for each Z_* and AGN model. (3) Total hydrogen density. (4) Ionization parameter ranging from −3.5 to −1.5 in increments of 0.2. (5) Covering factor, where 1.0 defines a closed geometry. (6) IMF upper mass limit for the SPs. (7) Power-law slopes of the IMFs and the AGN models. (8) Star formation histories. (9) Age of the SPs.
[a] The continuum shape given by the `table agn` command from CLOUDY is described in Table 6.3 of Hazy, the CLOUDY documentation.

(Senchyna et al. 2017). We therefore expect these conditions may also exist in z7_GND_42912. For each CLOUDY output, we redshifted the spectrum to $z_{\rm sys} = 7.5032$, and integrated them with the IRAC 3.6 and 4.5 μm bandpasses (following Papovich et al. 2001).

Figure 7 shows the various CLOUDY model results as a function of ionization parameter (for fixed model age of 10 Myr) compared to the measurements for z7_GND_42912, assuming both C III] line identifications, as in Figure 5. Models with older stellar-population ages are not shown as they produce relatively weaker lines (for a given U), and are unable to match the observed properties of z7_GND_42912, except for the most extreme case of BPASS binary SPs with an IMF that extends up to 300 $M_\odot$. If we allow for a lower C/O abundance ratio (compared to our assumed solar value), then the $W_{\rm C\,III]}$ would be lower for all models (see discussions of Gutkin et al. 2016 and Jaskot & Ravindranath 2016, who consider changes in abundance ratios in low metallicity high-redshift sources).

As illustrated in Figure 7, SP models that lack binaries and very high-mass stars have difficulty simultaneously producing the measured $W_{\rm C\,III]}$ and IRAC [3.6]–[4.5] color. Neither the S99 nor the BPASS models without binaries with an IMF that extends to 100 $M_\odot$ can reproduce the observed data—unless the nebular gas has a very low metallicity (<0.1 $Z_\odot$), and very high ionization (log $U \gtrsim -1.5$), and then only if the IRAC color lies at the lower end of its error distribution. BPASS models that include the stellar binaries and/or an upper mass of the IMF that extends to $M_{\rm IMF}^{\rm up} = 300\,M_\odot$ produce harder spectra and better match the observed $W_{\rm C\,III]}$ and [3.6]–[4.5] color over a larger range of ionization parameter, log $U = -2.1$ to −1.5. These models, which include the effects of stellar binaries, favor lower metallicity for both the ionizing SP and the nebular gas, with $Z \simeq 0.1$–$0.3\,Z_\odot$. All the models strongly disfavor higher metallicity, >0.5 $Z_\odot$, for either the stellar or gas components as these would produce much lower $W_{\rm C\,III]}$ than observed. Therefore, the data favor BPASS models with binaries with an IMF that extends to higher-mass stars and low metallicities. The effects of dust attenuation do not change these conclusions. While these were our youngest models, using SP models younger than 10 Myr would also produce higher ionization, resulting in more models that could possibly reach into the space occupied by this galaxy.

The results of our models are consistent with other work in the literature. In a series of simulations using CLOUDY and various S99 and BPASS SP models, Jaskot & Ravindranath (2016) found that $W_{\rm C\,III]}$ increased with increasing U at all Z_*. $W_{\rm C\,III]}$ was also found to slightly increase with increasing nebular density (traced by total hydrogen density), which follows the assumption that C III] traces denser regions (also related to a higher U; e.g., Jaskot & Ravindranath 2016; Sanders et al. 2016; Steidel et al. 2016; Berg et al. 2018). The youngest models in our sample (10 Myr) fit within Jaskot & Ravindranath's expected range for strong $W_{\rm C\,III]}$ with a fairly high ionization parameter (log $U \geqslant -2$) and continuous star formation, as well as lending weight to the notion that binary stellar evolution may be necessary to effectively reproduce these observed properties (also suggested by e.g., Steidel et al. 2016).[17] A similar result was found at lower redshifts by Berg et al. (2018) with a $z \sim 2$ lensed galaxy, with a best fit model involving binary stars, log $U = -1.5$, $Z = 0.05\,Z_\odot$, and an age of 10 Myr (however their models used BPASS SPs with an instantaneous burst instead of continuous star formation).

We also considered ionization in z7_GND_42912 from an active galactic nucleus (AGN), as this could boost both the C III] and [O III] emission (e.g., Jaskot & Ravindranath 2016; Maseda et al. 2017). From the the deep G102 grism data from FIGS (Pirzkal et al. 2017), T16 find tentative evidence for weak N V emission in z7_GND_42912, which could suggest ionization from a weak AGN (however, this N V emission was not detected by the >16 hr Keck/MOSFIRE spectrum in J19). We ran AGN models using CLOUDY's `table agn`[18] SED, with parameter values and ranges listed in Table 3.

None of the AGN models simultaneously produce the $W_{\rm C\,III]}$ and IRAC color as measured in z7_GND_42912. The bottom-right panel of Figure 7 shows the expected $W_{\rm C\,III]}$ and IRAC

[17] Note that our models assume solar abundance ratios (specifically, C/O = 0.51) and continuous star formation. These produce a higher C III] equivalent width compared to either models with lower abundance ratios (C/O) or instantaneous burst star formation, see, for example, discussion in Jaskot & Ravindranath (2016, their Figures 4 and 16).
[18] Described by Table 6.3 of Hazy, the CLOUDY documentation.

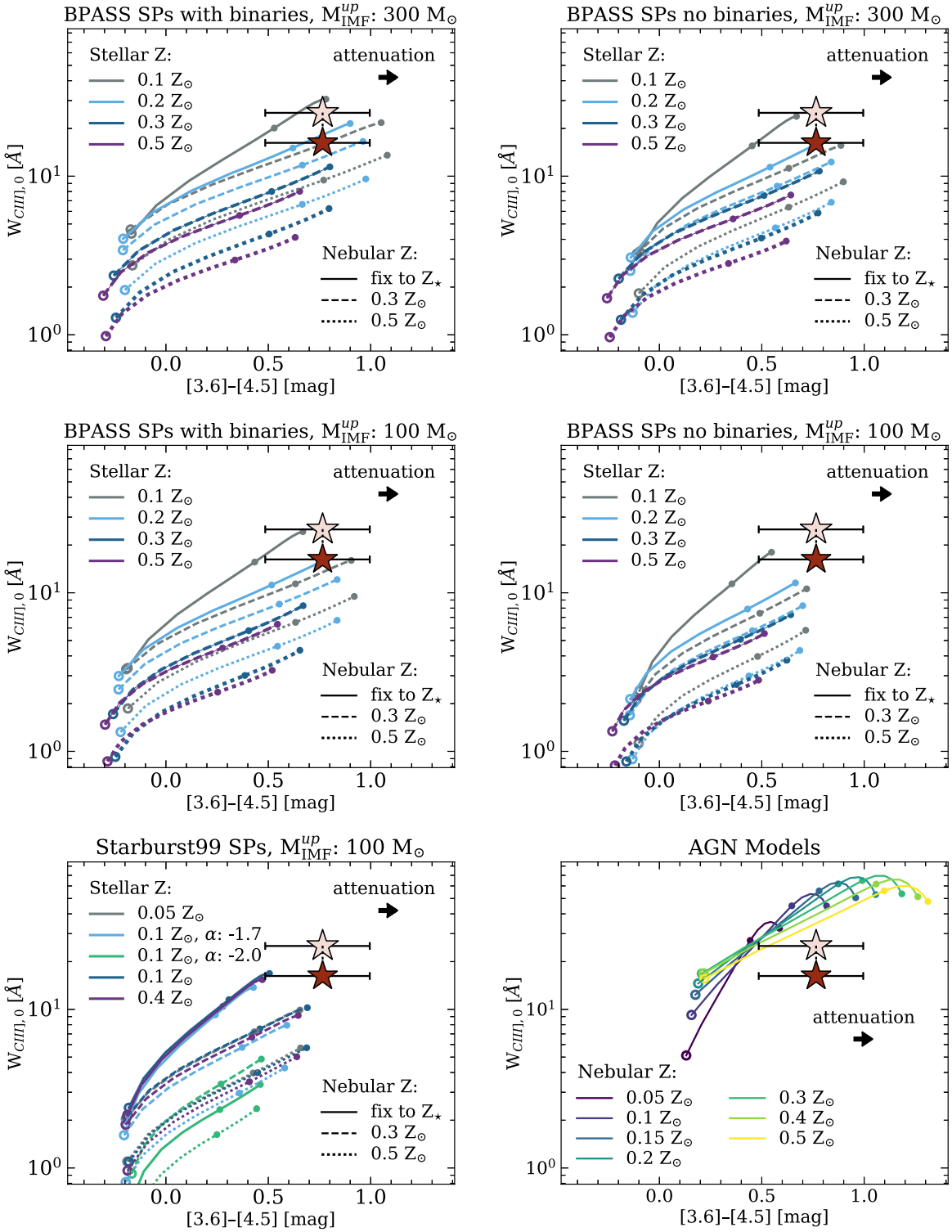

Figure 7. Rest-frame equivalent width of the C III] doublet vs. IRAC color. The large stars represent z7_GND_42912 where the dark red (light red) star assumes the detected emission is [C III] λ1907 (C III] λ1909). The lines show models as a function of ionization parameter, stellar metallicity, and nebular metallicity for the single and binary BPASS SPs with $M^{up}_{IMF} = 100$, 300 $M_\odot$, and the S99 SPs with $M^{up}_{IMF} = 100$ $M_\odot$. In the last panel, the CLOUDY AGN models are shown, following the parameters listed in Table 3. Each line shows the full range of ionization parameter explored (−3.5 to −1.5), with −3.5 indicated by the open circles and −2.5, −1.5 by the small circles. All of the SP models have continuous star formation with ages of 10 Myr. The IRAC color was measured by redshifting the model spectra to z_{sys} assuming the detected emission is [C III] λ1907 (but using the redshift for C III] λ1909 does not change the results). The solid black arrow shows the effect of dust attenuation using the reported $E(B-V)$ for z7_GND_42912, as described by Calzetti et al. (2000).

[3.6]–[4.5] color for the CLOUDY runs with the AGN spectrum for a range of gas metallicity and ionization parameter. To reproduce the IRAC color observed in z7_GND_42912, it requires higher ionization, which overproduces $W_{C\,III]}$ for these models. Some of this is mitigated if the line detected is C III] λ1909, and the IRAC color is at the low end of its error distribution (or if there is substantially more dust than inferred from the analysis of the SED, see F13). Therefore, it seems

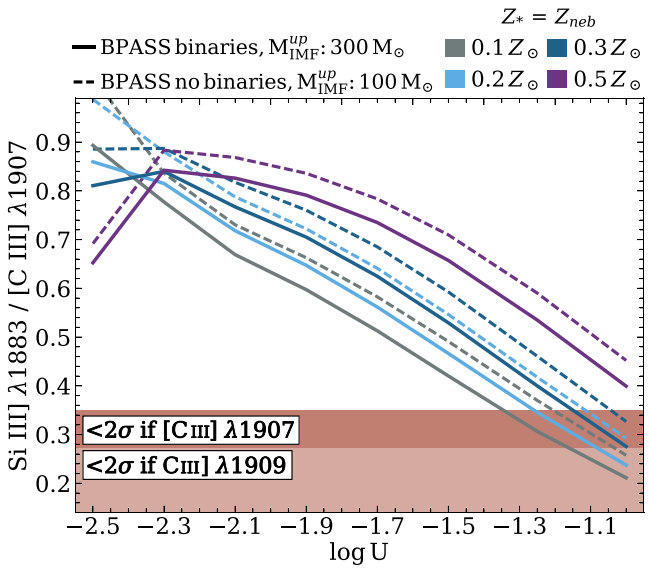

Figure 8. Ratio of Si III] λ1883/[C III] λ1907 vs. ionization parameter for our fiducial BPASS+CLOUDY models with continuous star formation and age of 10 Myr. The solid lines show models that include binaries with an IMF that extends to 300 $M_\odot$, and the dashed lines shows models without binaries and an IMF that extends to 100 $M_\odot$. The line colors match the stellar metallicities shown in Figure 7, and the shaded regions represent the 2σ upper limits for this ratio assuming the two different z_{sys} solutions.

unlikely that the ionization in z7_GND_42912 is powered solely by an AGN. One possibility is that the ionization in z7_GND_42912 is powered by a composite star-forming SP and an AGN. This has been observed in some galaxies. For their sample of $z = 2$–4 C III]-emitters, Nakajima et al. (2018b) found that high $W_{\rm C\,III]}$ ($\geqslant$20 Å) required a composite model of AGN and SPs to fit this and other galaxy properties. The presence of an AGN in z7_GND_42912 would have interesting implications for galaxies at $z > 6.5$, as some ionization from AGN may be required for the latter half of reionization (e.g., Finlator et al. 2016; Mitra et al. 2018; Finkelstein et al. 2019). The current data set for z7_GND_42912 prevents exploring more complex models (such as an AGN/stellar composite), but future studies (e.g., with *JWST*) will allow this.

The photoionization models make predictions for other nebular emission lines that could be present, including Si III] λ1883, for which we place an upper limit on the line flux from the MOSFIRE *H*-band spectrum (see above). Figure 8 compares our observed Si III]/[C III] limit to the predicted values from our youngest CLOUDY models (10 Myr). For solar abundances, the photoionization models produce a ratio of (Si III] λ1883)/([C III] λ1907) that varies over a range of 0.4–1.0 (for $-3.5 < \log U < -1.5$), higher than our measured upper limit. Indeed, the measured limit (2σ) on the ratio, Si III]/[C III] < 0.35, requires both high ionization ($\log U \gtrsim -1.5$) and lower metallicity ($Z \simeq 0.1 - 0.2\ Z_\odot$). We note that the results from the photoionization modeling assume solar abundance ratios. Using a lower (subsolar) [Si/C] abundance could also reduce the Si III]/[C III] flux ratio (as found by Berg et al. 2018) bringing the models more in line with the data. Therefore, the lack of detected Si III] supports the conclusion that the overall ionization in z7_GND_42912 must be extremely high combined with lower metallicity. This is consistent with the results derived from the analysis of the total C III] equivalent width and IRAC [3.6]–[4.5] color, above.

To summarize, z7_GND_42912 appears to require a hard ionizing SP and lower metallicity to reproduce the total C III] equivalent width and IRAC [3.6]–[4.5] color. The data further suggest that abundances of z7_GND_42912 for elements like silicon are subsolar compared to carbon and oxygen, consistent with other findings at $z \sim 2$ (e.g., Berg et al. 2018). In-depth studies must await additional data from facilities such as the *JWST*.

4.3. *Predictions for* JWST

The data for z7_GND_42912 favor SP models with high-mass stars, as in the BPASS models with an IMF that extends up to 300 $M_\odot$, binary SPs, and lower metallicities. This fits well with current expectations that galaxies in the early universe are younger, more metal-poor systems (e.g., Jaskot & Ravindranath 2016; Stark et al. 2015b; Steidel et al. 2016; Berg et al. 2018). However, alternative explanations remain. To test our conclusions, we make predictions for the advanced capabilities of future instruments such as NIRSpec on the *JWST*. The different models make strongly varying predictions for nebular emission expected for this galaxy. Detecting strong He II and N V emission could provide insight into the nature of the ionizing source of z7_GND_42912, allowing a more definitive distinction between the nature of the SPs, the presence of an obscured AGN, the combination of the two, or something wholly unexpected.

We make predictions for *JWST*/NIRSpec using our fiducial model (model 1; BPASS models with binaries with an IMF that extends to 300 $M_\odot$, constant SFR for an age of 10 Myr, and $Z_* = 0.2\ Z_\odot$) that matched the galaxy's ionization conditions as well as three other models. These include another SP model (model 2) with no binaries, an IMF that extends to 100 $M_\odot$, and matched parameters to our fiducial model (for comparison), and two AGN models from our analysis above with CLOUDY parameters, (model 3) $\log U = -1.7$, $Z_{\rm neb} = 0.5\ Z_\odot$, and (model 4) $\log U = -2.3$, $Z_{\rm neb} = 0.3\ Z_\odot$. In both models 1 and 2, we set the SP+CLOUDY models to have $\log U = -2.1$ and $Z_* = Z_{\rm neb} = 0.2\ Z_\odot$. We run these models through the *JWST* exposure time calculator (ETC)[19] via the `Python` Pandeia Engine[20] using slitted spectroscopy on NIRSpec. The continuum emission in the spectra were redshifted to our measured systemic value, $z_{\rm sys} = 7.5032$, with flux density normalized to match the updated *HST* F160W magnitude for z7_GND_42912 ($H_{160} = 25.38$ AB mag; Finkelstein et al. 2019, in preparation). We used a fixed slit setup with the prism and medium resolution gratings for the ETC runs, setting each "target" spectrum in its own scene. The background noise was set to medium.

Figure 9 shows simulated prism spectra for z7_GND_42912 for NIRSpec with an exposure time of 2 hr. Inset panels in the figure showed detail around the wavelengths where we expect N V and C III], assuming medium resolution gratings (G140M, G235M, G395M; see top part of Figure 9) for (longer) exposure times of 10 hr. Table 4 provides the predicted line fluxes relative to Hβ for each model. Even at the coarse spectroscopic resolution of the prism, it will be possible to measure simultaneously C III], [O III], and Lyα. In particular, Hβ and [O III] will be resolved, answering most of the questions about the nature of the ionization as the expected ratio of [O III]/Hβ is expected to be $\simeq$2$\times$higher for an AGN (see

[19] https://jwst.etc.stsci.edu
[20] https://jwst-docs.stsci.edu/display/JPP/Pandeia+Quickstart

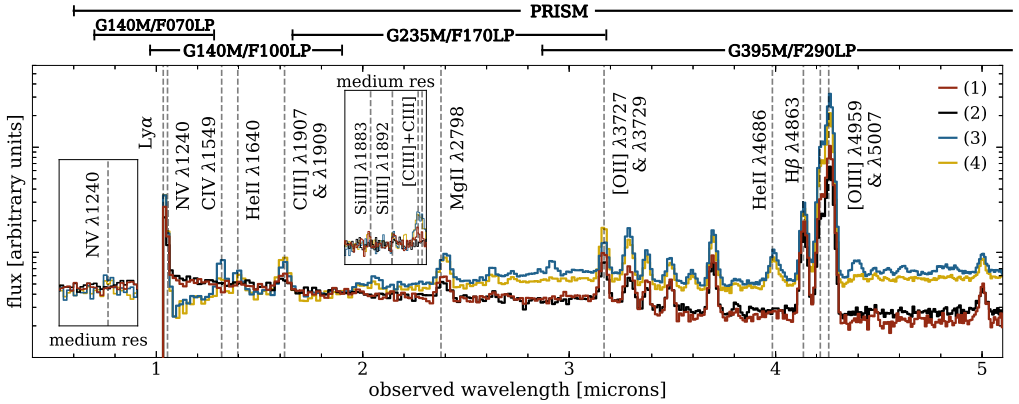

Figure 9. Simulated 1D spectra for z7_GND_42912 for a 2 hr (prism) and a 10 hr integration (zoom-in on N V and Si III] + C III] in the insets) using NIRSpec on *JWST*. (1) Our fiducial SP+CLOUDY model with binaries, $M_{\rm IMF}^{\rm up} = 300\ M_{\odot}$, $\log U = -2.1$ and $Z_{*} = Z_{\rm neb} = 0.2\ Z_{\odot}$. (2) An SP+CLOUDY model with no binaries, $M_{\rm IMF}^{\rm up} = 100\ M_{\odot}$, and matched $\log U$, Z_{*}, and $Z_{\rm neb}$ to our fiducial model. The two AGN models have (3) $\log U = -1.7$ and $Z_{\rm neb} = 0.5\ Z_{\odot}$, and (4) $\log U = -2.3$ and $Z_{\rm neb} = 0.3\ Z_{\odot}$. Major lines of interest are labeled, and the spectral coverage for the prism and medium resolution gratings are shown at the top.

Table 4
Estimated Line Fluxes Relative to Hβ for CLOUDY+SP/AGN Models with the *JWST*/NIRSpec $R \sim 100$ Prism

Model	C IVλ1548	He IIλ1640	Si III]λ1883,1892+ C III]λ1907,1909	Mg IIλ2798	[O II]λ3727,3729	He IIλ4686	Hβ	[O III]λ4959	[O III]λ5007
(1)	⋯	$0.05^{+0.03}_{-0.02}$	$0.30^{+0.12}_{-0.05}$	$0.29^{+0.03}_{-0.05}$	$0.43^{+0.02}_{-0.02}$	$0.15^{+0.03}_{-0.03}$	1.00	$1.82^{+0.04}_{-0.04}$	$5.55^{+0.08}_{-0.11}$
(2)	⋯	$0.07^{+0.02}_{-0.03}$	$0.42^{+0.11}_{-0.11}$	$0.26^{+0.03}_{-0.03}$	$0.47^{+0.03}_{-0.02}$	$0.18^{+0.04}_{-0.04}$	1.00	$1.56^{+0.05}_{-0.03}$	$4.73^{+0.09}_{-0.12}$
(3)	$0.32^{+0.03}_{-0.02}$	$0.22^{+0.49}_{-0.03}$	$0.28^{+0.02}_{-0.02}$	$0.33^{+0.02}_{-0.02}$	$0.30^{+0.01}_{-0.01}$	$0.34^{+0.02}_{-0.02}$	1.00	$4.15^{+0.05}_{-0.05}$	$12.48^{+0.12}_{-0.16}$
(4)	$0.18^{+0.06}_{-0.04}$	$0.23^{+0.05}_{-0.05}$	$0.45^{+0.02}_{-0.03}$	$0.37^{+0.02}_{-0.02}$	$0.63^{+0.02}_{-0.01}$	$0.30^{+0.03}_{-0.02}$	1.00	$3.04^{+0.03}_{-0.04}$	$9.23^{+0.1}_{-0.12}$

Note. The line flux ratios (relative to Hβ) shown are the median, 16th percentile, and 84th percentile measurements based upon our 2 hr *JWST*/NIRSpec $R \sim 100$ prism simulations. (1) Fiducial SP+CLOUDY model with binaries and $M_{\rm IMF}^{\rm up} = 300\ M_{\odot}$, $\log U = -2.1$ and $Z_{*} = Z_{\rm neb} = 0.2\ Z_{\odot}$. (2) SP+CLOUDY model with no binaries and $M_{\rm IMF}^{\rm up} = 100\ M_{\odot}$, $\log U = -2.1$ and $Z_{*} = Z_{\rm neb} = 0.2\ Z_{\odot}$. (3) AGN model with $\log U = -1.7$ and $Z_{\rm neb} = 0.5\ Z_{\odot}$. (4) AGN model with $\log U = -2.3$ and $Z_{\rm neb} = 0.3\ Z_{\odot}$.

Table 4). It may also be possible to determine spatially varying ionization. The higher resolution NIRSpec gratings (G140M/G140H, G235M/G235H, and G395M/G395H) should be able to differentiate between these lines with resolving powers of $R \simeq 1000$ and $R \simeq 2700$, respectively. At the higher resolution, more features become distinguishable such as the Si III] λ1883,1893 doublet, where comparisons to lines such as C III] allow for accurate constraints on the gas density and Si/C abundances (e.g., Steidel et al. 2016; Berg et al. 2018).

Detections of these lines and any spatial variation in their intensity would further constrain several important properties of this galaxy. Identification of certain spectral features such as N V and C IV would point more explicitly toward a contribution from an AGN. Resolved measurements of UV diagnostic lines C III], C IV, and He II (e.g., Villar-Martin et al. 1997; Feltre et al. 2016; Nakajima et al. 2018b) would independently label the ionizing source as a young actively star-forming galaxy, or an obscured (possibly weakly) accreting AGN, or possibly a composite of the two.

5. Summary

Using Keck/MOSFIRE *H*-band spectroscopy of a galaxy at $z_{{\rm Ly}\alpha} = 7.51$, previously identified via Lyα emission by Finkelstein et al. (2013), we identified line emission that we associate with one component of the C III] $\lambda\lambda$1907,1909 doublet at $\lambda_{\rm obs} = 1.6213\ \mu$m. We optimally extracted the 1D spectrum and measured a line flux of $(2.63 \pm 0.52) \times 10^{-18}$ erg s^{-1} cm^{-2}, with S/N = 5.6 integrated over the line. We do not detect Si III] $\lambda\lambda$1883, 1892, which yields an upper limit on the line ratio, Si III]/C III] < 0.35 (2σ).

Using the CANDELS photometry and Lyα measurement, we tentatively identified the detected line as the [C III] λ1907 part of the C III] doublet, providing a systemic redshift, $z_{\rm sys} = 7.5032 \pm 0.0003$. This resulted in $\Delta v_{{\rm Ly}\alpha} = 88 \pm 27$ km s^{-1}, suggesting that z7_GND_42912 potentially has significant hard radiation responsible for ionizing neutral H I gas in the vicinity of this galaxy, which would otherwise shift the Lyα emission further redwards from $z_{\rm sys}$. The low $\Delta v_{{\rm Ly}\alpha}$ instead implies that the Lyα emission remains fairly unaffected by H I until it encounters the IGM, suppressing the strength of the emission. In addition the hard radiation could be boosting C III] emission, making the ([C III] +C III])/Lyα ratio one of the highest measured for high-redshift sources.

To investigate the properties of z7_GND_42912 further, we modeled the expected total C III] equivalent width and IRAC [3.6]–[4.5] color using models (where the IRAC color is a measure of the redshifted Hβ + [O III] emission). We explored both BPASS and S99 SP models, and AGN power-law models, using the CLOUDY radiative transfer code to predict the nebular emission. We used a range of input stellar models, both single and binary SPs, with a range of stellar and nebular metallicities, SP age and ionization parameters.

The models that best reproduce the observed $W_{\rm C\,III]}$ and IRAC [3.6]–[4.5] color require SPs with models like in BPASS that include both the contributions from binary stars and an IMF that extends up to $M_{\rm IMF}^{\rm up} = 300\ M_{\odot}$, low stellar metallicity $Z_{*} = 0.1$–$0.2\ Z_{\odot}$, low nebular metallicity $Z_{\rm neb} = 0.2$–$0.3\ Z_{\odot}$,

and high ionization parameter $\log U \gtrsim -2$. The upper limit on Si III]/C III] requires even higher ionization, $\log U \gtrsim -1.5$, combined with lower metallicty, $Z \simeq 0.1$–$0.2\ Z_{\odot}$. The pure AGN models do not reproduce simultaneously the $W_{\rm C\,III]}$ and [3.6]–[4.5] color, but we cannot rule out a possible composite model including both an SP plus an AGN component.

The nature of the ionizing source(s) of z7_GND_42912 will be differentiable with forthcoming spectroscopy from the *JWST*. To make predictions for such data, we simulated *JWST* spectra for this galaxy using the closest models for z7_GND_42912 for both the case of ionization by SPs or AGNs and an additional comparison model. Even the coarse spectroscopy ($R \sim 100$) will resolve Hβ and [O III], where we expect large differences in the flux ratio depending on the nature of the ionization. Other observations at higher resolution will also be able to separate close doublets (such as C III]) and constrain better the metallicity, nature of the ionization, and its spatial variation, opening a new window into the nature of galaxies in the EoR.

The authors wish to recognize and acknowledge the very significant cultural role and reverence that the summit of Maunakea has always had within the indigenous Hawaiian community. We are most fortunate to have the opportunity to conduct observations from this sacred mountain. The authors thank R. Kennicutt, D. Stark, A. Jaskot, S. Ravindranath, D. Berg, and J. Cohn for insightful conversations and for constructive comments on the draft. We thank the anonymous reference for comments that improved this paper. T.A.H. and C.J.P. acknowledge generous support from the Texas A&M University and the George P. and Cynthia Woods Institute for Fundamental Physics and Astronomy. SLF acknowledges support from NSF AAG award AST-1518183. I.J. acknowledges support from the NASA Headquarters under the NASA Earth and Space Science Fellowship Program-Grant 80NSSC17K0532. R.S.E. acknowledges funding from the European Research Council (ERC) under the European Union's Horizon 2020 research and innovation programme (grant agreement No. 669253). S.M. and J.E.R. acknowledge support from NSF AAG award 1518057.

This work was supported by a NASA Keck PI Data Award, administered by the NASA Exoplanet Science Institute. Data presented herein were obtained at the W. M. Keck Observatory from telescope time allocated to the National Aeronautics and Space Administration through the agency's scientific partnership with the California Institute of Technology and the University of California. The Observatory was made possible by the generous financial support of the W. M. Keck Foundation.

Appendix

The following text concerns the data analysis used in this work. Due to the low S/N of these data, we believe this is important to share. This section is separated into two subsections. Appendix A discusses how we measured the photometric variability of our data for each observational epoch, and Appendix B discusses our method for calculating the optimized error for each data set.

Appendix A
Photometric Variability

The photometric variability for each epoch was determined by measuring the peak counts and the full width half maximum (FWHM) of the spatial profile of the "reference star" in the mask in each raw 120–180 s frame. To measure the values, we chose a region along the raw 2D spectra devoid of skylines to sum over in order to increase the signal—the same region was used for all 2014 data, while a similar region was chosen for the 2017 data. Figure 10 shows the results of the 2014 March 15 variability (left), with the 2017 April 18 data (right) shown for comparison. Overplotted on both are the measured airmasses over the full exposure and the average seeing, measured from the FWHM of the spatial profile of the final reduced 2D spectra for the reference star from each mask.

On a night with fair to good seeing, one would expect the peak counts and seeing to remain relatively constant; on a night with significant clouds or other atmospheric effects, the peak counts may vary wildly, with the seeing either remaining fairly constant or varying inversely to the peak counts. As can be seen in the left panel of Figure 10, the 2014 March 15 data showed significant variability in peak counts per raw frame—with persistent poor seeing averaging to $1\farcs03$, growing worse as the target field approached zenith. For comparison, the 2017 April 18 data showed some variability in peak counts, but not at all to the degree shown for the former data set. In addition, the seeing remained fairly constant, averaging to $0\farcs602$. Due to this evidence, we determined that the 2014 March 15 data should be left out of the analysis so as to not add unnecessary noise to our measurements.

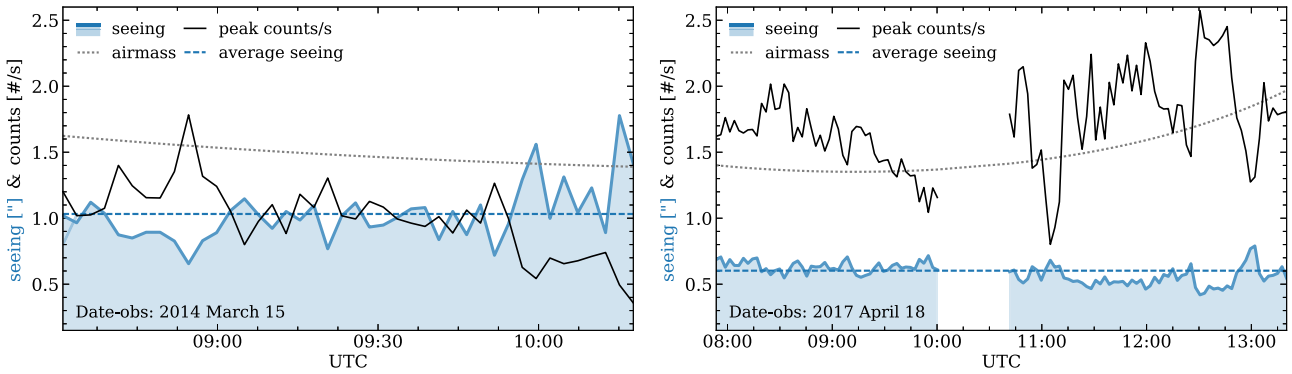

Figure 10. Peak counts and seeing (measured from FWHM of the spatial profile of the reference star) for each raw data frame for 2014 March 15 and 2017 April 18. Overplotted are the airmass and average seeing (measured from the final reduced 2D spectra of the reference star). Due to the significant variability in peak counts and the poor seeing, the 2014 March 15 data were left out of the analysis.

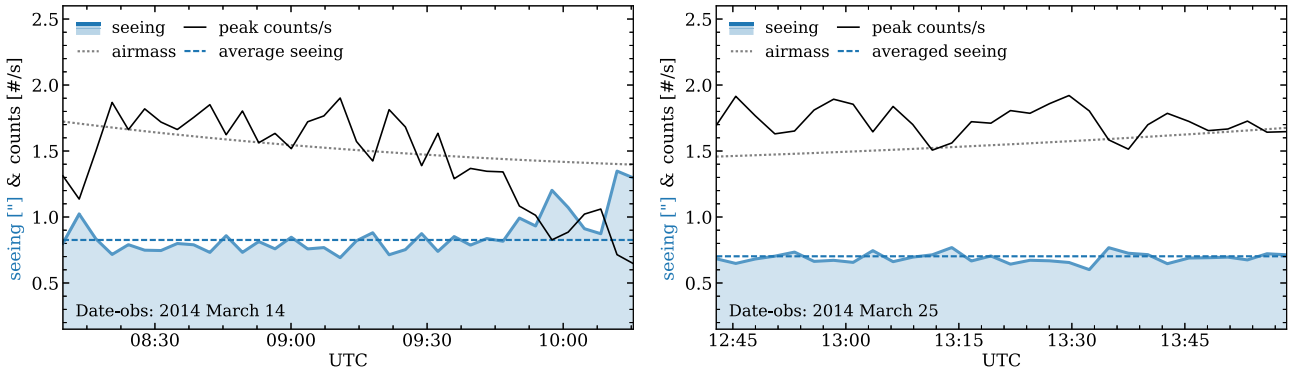

Figure 11. Peak counts and seeing (measured from FWHM of the spatial profile of the reference star) for each raw data frame for 2014 March 14 & 25. Overplotted are the airmass and average seeing (measured from the final reduced 2D spectra of the reference star). Due to the significant variability in peak counts from the median, only 08:20–09:30 UTC from the 2014 March 14 data were used in the analysis.

In addition to that epoch, a handful of frames were removed from the 2014 March 14 data where the peak counts varied significantly from the median. Figure 11 shows these fluctuations in the 2014 March 14 data (left), as well as the pristine 2014 March 25 data (right). Due to these results, we only used 08:20–09:30 UTC from the 2014 March 14 data.

Appendix B
Optimized 1D Error

For the optimized 1D error associated with the optimized 1D spectra, we used an alternative approach than described by Horne (1986). Due to the nature of the multi-slit mask of targets created by MOSFIRE, we calculated an error that would be applicable for every object in the mask. First, as this was primarily a search for high-redshift galaxies, a few of our targets yielded nondetections, providing full slit space to utilize for our optimized error.

Following the same optimized 1D extraction technique developed and used on our target spectra, we optimally extracted "blank" apertures in these regions in the full mask devoid of any discernible signal or negative trace (unique to spectrographs like MOSFIRE). Building a statistical sample of these "blank" apertures, we then plotted their distribution at each wavelength step and used the resulting standard deviation as the error at that wavelength step. The left panel of Figure 12 shows all of the "blank" apertures for the 2017 April 18 data—as expected the resulting spectra only shows the skylines and noise of the data. The right panel of Figure 12 shows an example of the distributions at different wavelength steps and their resulting statistics.

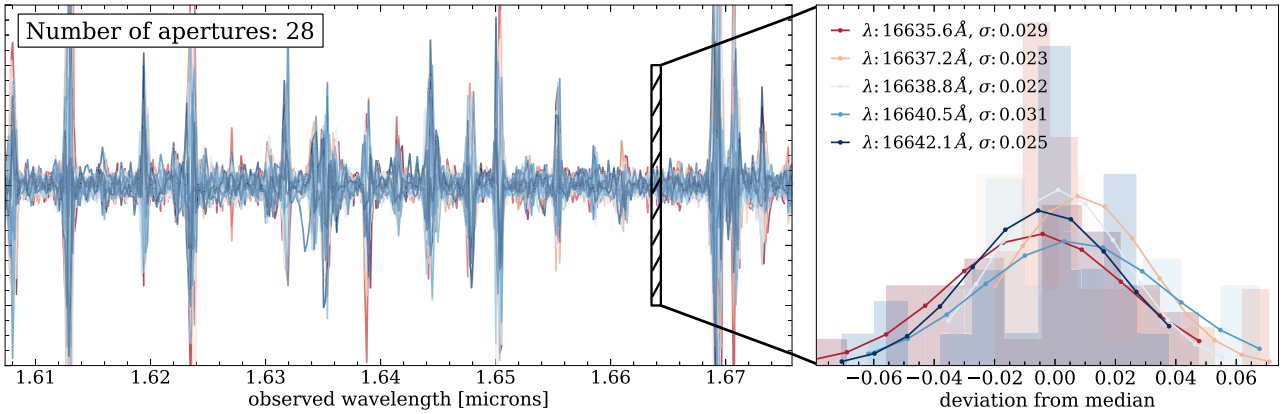

Figure 12. Left: a zoom-in of a section of the spectral range for the "blank" spectra for the 2017 April 18 data, showing noise and skylines. The hatched rectangle indicates the spectral range shown on the right. Right: section of "blank" spectra showing the distribution of the apertures and the standard deviation from the median value of counts per wavelength step.

ORCID iDs

Taylor A. Hutchison https://orcid.org/0000-0001-6251-4988
Casey Papovich https://orcid.org/0000-0001-7503-8482
Steven L. Finkelstein https://orcid.org/0000-0001-8519-1130
Intae Jung https://orcid.org/0000-0003-1187-4240
Adi Zitrin https://orcid.org/0000-0002-0350-4488
Sangeeta Malhotra https://orcid.org/0000-0002-9226-5350
James Rhoads https://orcid.org/0000-0002-1501-454X
Guido Roberts-Borsani https://orcid.org/0000-0002-4140-1367
Mimi Song https://orcid.org/0000-0002-8442-3128
Vithal Tilvi https://orcid.org/0000-0001-8514-7105

References

Bañados, E., Venemans, B. P., Mazzucchelli, C., et al. 2018, Natur, 553, 473
Berg, D. A., Erb, D. K., Auger, M. W., Pettini, M., & Brammer, G. B. 2018, ApJ, 859, 164
Bouwens, R. J., Illingworth, G. D., Oesch, P. A., et al. 2015, ApJ, 803, 34
Byler, N., Dalcanton, J. J., Conroy, C., et al. 2018, ApJ, 863, 14
Byler, N., Dalcanton, J. J., Conroy, C., & Johnson, B. D. 2017, ApJ, 840, 44
Calzetti, D., Armus, L., Bohlin, R. C., et al. 2000, ApJ, 533, 682
Chonis, T. S., Blanc, G. A., Hill, G. J., et al. 2013, ApJ, 775, 99
Choudhury, T. R., Puchwein, E., Haehnelt, M. G., & Bolton, J. S. 2015, MNRAS, 452, 261
Dayal, P., & Ferrara, A. 2018, PhR, 780, 1
Dijkstra, M. 2014, PASA, 31, e040
Dijkstra, M. 2017, arXiv:1704.03416
Ding, J., Cai, Z., Fan, X., et al. 2017, ApJL, 838, L22
Du, X., Shapley, A. E., Reddy, N. A., et al. 2018, ApJ, 860, 75
Eldridge, J. J., Stanway, E. R., Xiao, L., et al. 2017, PASA, 34, e058
Erb, D. K., Pettini, M., Shapley, A. E., et al. 2010, ApJ, 719, 1168
Erb, D. K., Steidel, C. C., Trainor, R. F., et al. 2014, ApJ, 795, 33
Fan, X., Narayanan, V. K., Strauss, M. A., et al. 2002, AJ, 123, 1247
Feltre, A., Charlot, S., & Gutkin, J. 2016, MNRAS, 456, 3354
Ferland, G. J., Chatzikos, M., Guzmán, F., et al. 2017, RMxAA, 53, 385
Finkelstein, S. L. 2016, PASA, 33, e037
Finkelstein, S. L., D'Aloisio, A., Paardekooper, J. P., et al. 2019, ApJ, submitted (arXiv:1902.02792)
Finkelstein, S. L., Papovich, C., Dickinson, M., et al. 2013, Natur, 502, 524
Finkelstein, S. L., Song, M., Behroozi, P., et al. 2015, ApJ, 814, 95
Finlator, K., Oppenheimer, B. D., Davé, R., et al. 2016, MNRAS, 459, 2299
Giavalisco, M., Ferguson, H. C., Koekemoer, A. M., et al. 2004, ApJL, 600, L93
Grogin, N. A., Kocevski, D. D., Faber, S. M., et al. 2011, ApJS, 197, 35
Gutkin, J., Charlot, S., & Bruzual, G. 2016, MNRAS, 462, 1757
Hainline, K. N., Shapley, A. E., Greene, J. E., & Steidel, C. C. 2011, ApJ, 733, 31
Hayes, M. 2015, PASA, 32, e027
Hayes, M., Östlin, G., Schaerer, D., et al. 2010, Natur, 464, 562
Hayes, M., Schaerer, D., Östlin, G., et al. 2011, ApJ, 730, 8
Horne, K. 1986, PASP, 98, 609
Inoue, A. K. 2011, MNRAS, 415, 2920
Jaskot, A. E., & Ravindranath, S. 2016, ApJ, 833, 136
Jung, I., Finkelstein, S. L., Dickinson, M., et al. 2019, ApJ, 877, 146
Kimm, T., Blaizot, J., Garel, T., et al. 2019, MNRAS, 486, 2215
Koekemoer, A. M., Faber, S. M., Ferguson, H. C., et al. 2011, ApJS, 197, 36
Kurucz, R. 1993, SYNTHE Spectrum Synthesis Programs and Line Data. Kurucz CD-ROM No. 18 (Cambridge, MA: Smithsonian Astrophysical Observatory), 18
Laporte, N., Ellis, R. S., Boone, F., et al. 2017a, ApJL, 837, L21
Laporte, N., Nakajima, K., Ellis, R. S., et al. 2017b, ApJ, 851, 40
Larson, R. L., Finkelstein, S. L., Pirzkal, N., et al. 2018, ApJ, 858, 94
Leitherer, C., Ekström, S., Meynet, G., et al. 2014, ApJS, 212, 14
Mainali, R., Kollmeier, J. A., Stark, D. P., et al. 2017, ApJL, 836, L14
Maseda, M. V., Brinchmann, J., Franx, M., et al. 2017, A&A, 608, A4
Mason, C. A., Treu, T., Dijkstra, M., et al. 2018, ApJ, 856, 2
Matthee, J., Sobral, D., Darvish, B., et al. 2017, MNRAS, 472, 772
Matthee, J., Sobral, D., Oteo, I., et al. 2016, MNRAS, 458, 449
McGreer, I. D., Mesinger, A., & D'Odorico, V. 2015, MNRAS, 447, 499
McLean, I. S., Steidel, C. C., Epps, H. W., et al. 2012, Proc. SPIE, 8446, 84460J
McLinden, E. M., Finkelstein, S. L., Rhoads, J. E., et al. 2011, ApJ, 730, 136
McLinden, E. M., Rhoads, J. E., Malhotra, S., et al. 2014, MNRAS, 439, 446
Mitra, S., Choudhury, T. R., & Ferrara, A. 2018, MNRAS, 473, 1416
Møller, P., & Warren, S. J. 1998, MNRAS, 299, 661
Mortlock, D. J., Warren, S. J., Venemans, B. P., et al. 2011, Natur, 474, 616
Nakajima, K., Fletcher, T., Ellis, R. S., Robertson, B. E., & Iwata, I. 2018a, MNRAS, 477, 2098
Nakajima, K., Schaerer, D., Le Fèvre, O., et al. 2018b, A&A, 612, A94
Oesch, P. A., van Dokkum, P. G., Illingworth, G. D., et al. 2015, ApJL, 804, L30
Oke, J. B., & Gunn, J. E. 1983, ApJ, 266, 713
Ono, Y., Ouchi, M., Mobasher, B., et al. 2012, AAS Meeting Abstracts, 220, 429.03
Papovich, C., Dickinson, M., & Ferguson, H. C. 2001, ApJ, 559, 620
Patrício, V., Richard, J., Verhamme, A., et al. 2016, MNRAS, 456, 4191
Pirzkal, N., Malhotra, S., Ryan, R. E., et al. 2017, ApJ, 846, 84
Planck Collaboration, Ade, P. A. R., Aghanim, N., et al. 2016, A&A, 594, A13
Riess, A. G., Macri, L. M., Hoffmann, S. L., et al. 2016, ApJ, 826, 56
Roberts-Borsani, G. W., Bouwens, R. J., Oesch, P. A., et al. 2016, ApJ, 823, 143
Sanders, R. L., Shapley, A. E., Kriek, M., et al. 2016, ApJ, 816, 23
Schenker, M. A., Ellis, R. S., Konidaris, N. P., & Stark, D. P. 2013, ApJ, 777, 67
Schenker, M. A., Ellis, R. S., Konidaris, N. P., & Stark, D. P. 2014, ApJ, 795, 20
Schenker, M. A., Stark, D. P., Ellis, R. S., et al. 2012, ApJ, 744, 179
Senchyna, P., Stark, D. P., Vidal-García, A., et al. 2017, MNRAS, 472, 2608

Shapley, A. E., Steidel, C. C., Pettini, M., & Adelberger, K. L. 2003, ApJ, 588, 65
Shibuya, T., Kashikawa, N., Ota, K., et al. 2012, ApJ, 752, 114
Smit, R., Bouwens, R. J., Franx, M., et al. 2015, ApJ, 801, 122
Sobral, D., Matthee, J., Best, P., et al. 2017, MNRAS, 466, 1242
Sobral, D., Matthee, J., Darvish, B., et al. 2018, MNRAS, 477, 2817
Song, M., Finkelstein, S. L., Ashby, M. L. N., et al. 2016, ApJ, 825, 5
Song, M., Finkelstein, S. L., Gebhardt, K., et al. 2014, ApJ, 791, 3
Stanway, E. R., Eldridge, J. J., Greis, S. M. L., et al. 2014, MNRAS, 444, 3466
Stark, D. P. 2016, ARA&A, 54, 761
Stark, D. P., Ellis, R. S., Charlot, S., et al. 2017, MNRAS, 464, 469
Stark, D. P., Richard, J., Charlot, S., et al. 2015a, MNRAS, 450, 1846
Stark, D. P., Richard, J., Siana, B., et al. 2014, MNRAS, 445, 3200
Stark, D. P., Walth, G., Charlot, S., et al. 2015b, MNRAS, 454, 1393
Steidel, C. C., Bogosavljević, M., Shapley, A. E., et al. 2011, ApJ, 736, 160
Steidel, C. C., Strom, A. L., Pettini, M., et al. 2016, ApJ, 826, 159
Strom, A. L., Steidel, C. C., Rudie, G. C., et al. 2017, ApJ, 836, 164
Tang, M., Stark, D., Chevallard, J., & Charlot, S. 2018, arXiv:1809.09637
Tilvi, V., Papovich, C., Finkelstein, S. L., et al. 2014, ApJ, 794, 5
Tilvi, V., Pirzkal, N., Malhotra, S., et al. 2016, ApJL, 827, L14
Treu, T., Schmidt, K. B., Trenti, M., Bradley, L. D., & Stiavelli, M. 2013, ApJL, 775, L29
Vanzella, E., Pentericci, L., Fontana, A., et al. 2011, ApJL, 730, L35
Venemans, B. P., Findlay, J. R., Sutherland, W. J., et al. 2013, ApJ, 779, 24
Verhamme, A., Orlitová, I., Schaerer, D., & Hayes, M. 2015, A&A, 578, A7
Verhamme, A., Schaerer, D., & Maselli, A. 2006, A&A, 460, 397
Villar-Martin, M., Tadhunter, C., & Clark, N. 1997, A&A, 323, 21
Willott, C. J., Carilli, C. L., Wagg, J., & Wang, R. 2015, ApJ, 807, 180
Yang, H., Malhotra, S., Gronke, M., et al. 2017, ApJ, 844, 171
Zitrin, A., Labbé, I., Belli, S., et al. 2015, ApJL, 810, L12